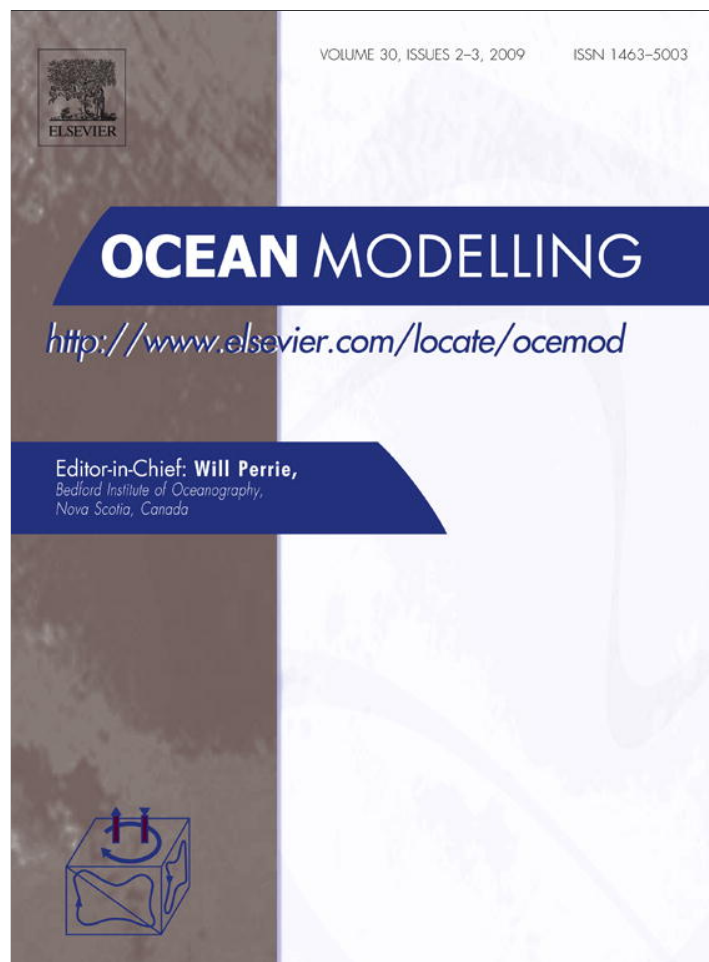


Provided for non-commercial research and education use.  
Not for reproduction, distribution or commercial use.



This article appeared in a journal published by Elsevier. The attached copy is furnished to the author for internal non-commercial research and education use, including for instruction at the authors institution and sharing with colleagues.

Other uses, including reproduction and distribution, or selling or licensing copies, or posting to personal, institutional or third party websites are prohibited.

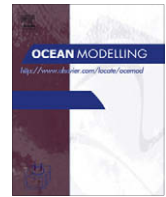
In most cases authors are permitted to post their version of the article (e.g. in Word or Tex form) to their personal website or institutional repository. Authors requiring further information regarding Elsevier's archiving and manuscript policies are encouraged to visit:

<http://www.elsevier.com/copyright>



Contents lists available at ScienceDirect

## Ocean Modelling

journal homepage: [www.elsevier.com/locate/ocemod](http://www.elsevier.com/locate/ocemod)

# Reynolds number dependence of mixing in a lock-exchange system from direct numerical and large eddy simulations

Tamay M. Özgökmen<sup>a,\*</sup>, Traian Iliescu<sup>b</sup>, Paul F. Fischer<sup>c</sup>

<sup>a</sup>RSMAS/MPO, University of Miami, Miami, FL, USA

<sup>b</sup>Department of Mathematics, Virginia Polytechnic Institute and State University, Blacksburg, VA, USA

<sup>c</sup>Mathematics and Computer Science Division, Argonne National Laboratory, Argonne, IL, USA

## ARTICLE INFO

### Article history:

Received 3 March 2009

Received in revised form 23 June 2009

Accepted 25 June 2009

Available online 9 July 2009

### Keywords:

LES

DNS

Reynolds number

Mixing

## ABSTRACT

Turbulent mixing of water masses of different temperatures and salinities is an important process for both coastal and large-scale ocean circulation. It is, however, difficult to capture computationally. One of the reasons is that mixing in the ocean occurs at a wide range of complexity, with the Reynolds number reaching  $Re = \mathcal{O}(10^6)$ , or even higher.

In this study, we continue to investigate whether large eddy simulation (LES) can be a reliable computational tool for stratified mixing in turbulent oceanic flows. LES is attractive because it can be  $\mathcal{O}(1000)$  times faster than a direct numerical simulation (DNS) of stratified mixing in turbulent flows. Before using the LES methodology to compute mixing in realistic oceanic flows, however, a careful assessment of the LES sensitivity with respect to  $Re$  needs to be performed first. The main objectives of this study are: (i) to investigate the performance of different LES models at high  $Re$ , such as those encountered in oceanic flows; and (ii) to study how mixing varies as a function of  $Re$ . To this end, as a benchmark we use the lock-exchange problem, which is described by unambiguous and simple initial and boundary conditions. The background potential energy, which accurately quantifies irreversible mixing in an enclosed system, is used as the main criterion in *a posteriori* testing of LES.

This study has two main achievements. The first is that we investigate the accuracy of six combinations of two different classes of LES models, namely eddy-viscosity and approximate deconvolution types, for  $3 \times 10^3 \leq Re \leq 3 \times 10^4$ , for which DNS data is computed. We find that all LES models almost always provide significantly more accurate results than cases without LES models. Nevertheless, no single LES model that is persistently superior to others over this  $Re$  range could be identified. Then, an ensemble of the four best performing LES models is selected in order to estimate mixing taking place in this system at  $Re = 10^5$  and  $10^6$ , for which DNS is presently not feasible. Thus the second achievement of this study is to quantify mixing taking place in this system over an  $Re$  range that changes by three orders of magnitude. We find that the background potential energy increases by about 67% when  $Re$  is increased from  $Re = 10^3$  to  $Re = 10^6$ , within the computation period, with the most significant increase taking place from  $Re = 3 \times 10^3$  to  $Re = 10^5$ .

© 2009 Elsevier Ltd. All rights reserved.

## 1. Introduction

Mixing in stratified flows is a fundamental area of research in oceanography because of the importance of this process in coastal regions, as well as in the surface mixed layer, subsurface flows near the equatorial zones (Kantha and Clayson, 2000; Thorpe, 2005), bottom flows such as overflows (Price and Baringer, 1994), and those interacting with topographic features such as ocean ridges (Poltzin et al., 1997; Ferron et al., 1998; Ledwell et al., 2000), sea mounts (Nabatov and Ozmidov, 1988; Gibson et al., 1993; Lueck and Mudge, 1997; Kunze and Toole, 1997; Lavelle et al., 2004),

steep continental slope (Moum et al., 2002) and canyons along the mid-ocean ridges (Thurnherr and Speer, 2003; Thurnherr et al., 2004; Thurnherr, 2006).

These oceanic flows can achieve high levels of turbulence, mainly because of their large spatial scale and high vertical shear. For instance, the thickness of stratified overturns in overflows or equatorial undercurrents can be on the order of 1–2 m, while the largest overturns seem to reach scales up to tens of meters (Table 1 in Peters and Johns (2005) and Fig. 5 in Peters et al. (1995)). Using  $\ell = 2$  m,  $U = 0.5$  ms<sup>-1</sup> and  $\nu = 10^{-6}$  m<sup>2</sup> s<sup>-1</sup>, we obtain  $Re = U\ell/\nu \approx 10^6$  as a typical turbulence regime for such mixing regions.

There are essentially two modern approaches for modeling stratified mixing for applications in oceanic flows. The first is the use of second-order closure (SOC) models that have shown a

\* Corresponding author.

E-mail address: [tozgekmen@rsmas.miami.edu](mailto:tozgekmen@rsmas.miami.edu) (T.M. Özgökmen).

steady improvement over the past few decades (Mellor and Yamada, 1982; Kantha and Clayson, 1994; Burchard and Baumert, 1995; Burchard and Bolding, 2001; Canuto et al., 2001; Baumert and Peters, 2004; Baumert et al., 2005; Warner et al., 2005; Umlauf and Burchard, 2005; Canuto et al., 2007; Ilıcak et al., 2008). The increasing computational power is making a new class of models feasible for oceanic applications as well. These models integrate the non-hydrostatic (Boussinesq) equations of motion, as opposed to hydrostatic (primitive) equations. In direct numerical simulation (DNS), these non-hydrostatic models allow simulation of fluid flow without any parameterization; in large eddy simulation (LES), only the effect of the small scales of turbulence is parameterized. In general, the LES models are considered to be more accurate than the SOC models, but this accuracy comes at a price. LES models are significantly more expensive computationally than the SOC models. Also, unlike the SOC models, LES models cannot be readily incorporated into existing codes of ocean general circulation models (OGCMs). The results from such non-hydrostatic simulations can still be used in OGCMs if they can be distilled in the form of a parameterization (Chang et al., 2005; Xu et al., 2006). It thus appears that LES and SOC models have complementary roles in the numerical simulation of turbulent oceanic flows: SOC is appropriate for parameterizations in OGCMs and large scale circulation modeling, whereas LES is appropriate for simulations of oceanic processes that cannot be resolved explicitly in OGCMs, and show promise even for coastal flow simulations.

Before using LES in realistic oceanic simulations, however, one needs to carry out a thorough testing of the LES methodology for stratified turbulent flows. The present study is a continuation of our previous attempts of testing several LES models in a benchmark setting for stratified turbulent flows, namely the lock-exchange problem (Özgökmen et al., 2007, 2009).

We have two main objectives in this study:

- (1) The first goal of this study is to investigate the sensitivity of LES results with respect to the Reynolds number  $Re$ , which is the ratio of inertial and viscous forces. The motivation behind our study is that the ocean displays a wide range of  $Re$ . Indeed, in many oceanic flows,  $Re$  can vary from several thousands to a million and higher. Since our ultimate goal is to gain insight into mixing in realistic, high  $Re$  oceanic flows, we first need to make sure that the LES results do not degrade with  $Re$ . Specifically, we must ensure that (i) the LES models accurately capture mixing in turbulent stratified flows; (ii) the LES computational cost is much (usually about 1000 times) lower than that of a DNS for the same accuracy; and (iii) the results in (i) and (ii) do not change when  $Re$  is increased.
- (2) The second goal of this study is to use both DNS and LES to understand how mixing changes for a wide range of  $Re$ , such as those found in the ocean. The primary physical question we try to address in this study is the following: What is the net effect of turbulence on mixing and how does mixing change as a function of  $Re$ ? Because of the heavy computational burden, we can only use DNS for a relatively modest  $Re$  range:  $10^3 \leq Re \leq 3 \times 10^4$ . Therefore, we use the LES models to investigate mixing at  $Re$  that are not computationally attainable with DNS:  $10^5 \leq Re \leq 10^6$ . Of course, in order to be scientifically validated, our conclusions based on LES must await further confirmation, either from physical experiments or from massive DNS (when these become feasible).

As a benchmark setting, we employ the popular lock-exchange problem in an enclosed box domain (Benjamin, 1968; Britter and Simpson, 1978; Simpson, 1979; Huppert and Simpson, 1980; Rottman and Simpson, 1983; Hallworth et al., 1993, 1996; Hacker et al.,

1996; Benjamin, 1968; Shin et al., 2004; Härtel et al., 2000; Cantero et al., 2006; Cantero et al., 2007; Özgökmen et al., 2007, 2009). This setting is characterized by simple and unambiguous boundary conditions, initial conditions and domain geometry, yet complex dynamics consisting of stably- and unstably-stratified mixing, internal waves, interactions with domain boundaries and transient states.

The study is conducted in three stages. First, we run DNS of the lock-exchange problem at increasing  $Re$ , namely at  $Re = 10^3$ ,  $Re = 3 \times 10^3$ ,  $Re = 10^4$  and  $Re = 3 \times 10^4$ . Mixing of the density perturbation is quantified using the background potential energy (Winters et al., 1995). We show that DNS is not feasible with the computational resources available to us for a larger  $Re$ . Then, we investigate the accuracy of several different SGS models for LES using the background potential energy from DNS computations as a metric for *a posteriori* testing. Finally, we rely on LES to explore mixing in this system at  $Re = 10^5$  and  $Re = 10^6$ .

In all our numerical experiments, we use Nek5000, a high-order spectral element code developed by Fischer (1997) and Fischer et al. (2000). The spectral element formulation combines the geometrical flexibility of finite element models with the numerical accuracy of spectral models in a way that is especially suitable for parallel computing environments. While the box-shaped domain does not employ the geometrical flexibility of this model, the high-order numerical accuracy is critical in avoiding numerical dissipation and dispersion errors.

The paper is organized as follows: The concept of LES and the SGS models tested in this study are discussed in Section 2. A short description of the numerical model Nek5000 is given in Section 3. The model configuration and the parameters of the numerical experiments are outlined in Section 4. Results are presented in Section 5. Finally, the principal findings and future directions are summarized in Section 6.

## 2. Large eddy simulation

The main concept behind LES is that turbulent flows tend to organize themselves in the form of so-called coherent structures, such as eddies, jets and filaments. Imbedded in these structures are smaller eddies that arise from the turbulent break down of the larger eddies. The coherent structures are highly dependent of the flow type and geometry while containing most of the turbulent kinetic energy and carrying out most of the mixing. The smaller features are considered to contribute far less to mixing but may play a more universal role, such as energy dissipation. In LES, the large eddies are resolved through computation and the effect of the small eddies on the resolved flow field is parameterized using SGS models. The reader is referred to Sagaut (2006) and Berselli et al. (2005) for an extensive review of recent LES literature.

Here, the equations of motion governing fluid motion are the Boussinesq equations:

$$\begin{cases} \frac{D\mathbf{u}}{Dt} + \frac{1}{\rho_0} \nabla p - \nu \Delta \mathbf{u} + \frac{\rho'}{\rho_0} \mathbf{g} \mathbf{k} = 0, \\ \nabla \cdot \mathbf{u} = 0, \\ \frac{D\rho'}{Dt} - \kappa \Delta \rho' = 0, \end{cases} \quad (1)$$

where  $\frac{D}{Dt} = \frac{\partial}{\partial t} + \mathbf{u} \cdot \nabla$  is the material (total) derivative,  $\Delta$  the Laplacian operator,  $\rho_0$  the constant fluid density,  $\rho'$  the density perturbation in a fluid with density  $\rho = \rho_0 + \rho'$  such that  $\rho' \ll \rho_0$ ,  $p$  the pressure,  $\nu$  the kinematic viscosity,  $\kappa$  the molecular diffusivity,  $\mathbf{g}$  the gravitational acceleration, and  $\mathbf{k}$  the unit normal vector in the vertical direction.

First, Boussinesq equations are non-dimensionalized for the lock-exchange problem using  $\mathbf{u} = U_0 \mathbf{u}^*$ ,  $\mathbf{x} = \ell \mathbf{x}^*$ ,  $t = \frac{\ell}{U_0} t^*$ ,  $p = \rho_0 U_0^2 p^*$ ,  $\rho' = \Delta \rho' \rho^{*}$ , where  $U_0$  and  $\ell$  are characteristic speed and length scales of the gravity currents, and  $\Delta \rho'$  is the density difference

between the two main water masses. In LES formalism, a spatial filtering function  $g_\delta(\mathbf{x})$  is applied to the equations of motion in order to suppress any fluctuation below the filter scale  $\delta$ . Namely  $\bar{\mathbf{u}}(\mathbf{x}, t) := (g_\delta * \mathbf{u})(\mathbf{x}, t)$ , and  $\bar{\rho}'(\mathbf{x}, t) := (g_\delta * \rho')(\mathbf{x}, t)$ . Dropping stars, the non-dimensionalized and filtered Boussinesq equations become:

$$\begin{cases} \frac{D\bar{\mathbf{u}}}{Dt} + \nabla \bar{p} - \frac{1}{Re} \Delta \bar{\mathbf{u}} + \frac{1}{Pe} \rho' \mathbf{k} = -\nabla \cdot \boldsymbol{\tau}(\mathbf{u}, \mathbf{u}), \\ \nabla \cdot \bar{\mathbf{u}} = 0, \\ \frac{D\bar{\rho}'}{Dt} - \frac{1}{Fr} \Delta \bar{\rho}' = -\nabla \cdot \boldsymbol{\sigma}(\mathbf{u}, \rho'), \end{cases} \quad (2)$$

where  $Re = U_0 \ell / \nu$  is the Reynolds number,  $Pe = U_0 \ell / \kappa$  is the Peclet number,  $Fr = U_0 / \sqrt{g \Delta \rho' \ell / \rho_0}$  is the Froude number, and

$$\boldsymbol{\tau}(\mathbf{u}, \mathbf{u}) = \bar{\mathbf{u}}\bar{\mathbf{u}} - \bar{\mathbf{u}}\bar{\mathbf{u}} \quad \text{and} \quad \boldsymbol{\sigma}(\mathbf{u}, \rho') = \bar{\mathbf{u}}\bar{\rho}' - \bar{\mathbf{u}}\bar{\rho}' \quad (3)$$

are the SGS tensors representing the net effect of unresolved scales of motion on the resolved fields. In DNS, all scales of motion are computed and the SGS terms vanish;  $\boldsymbol{\tau} = 0$ ,  $\boldsymbol{\sigma} = 0$ . We refer to an under-resolved simulation without SGS terms as DNS<sup>\*</sup>. LES is then a coarse mesh simulation in which SGS models are explicitly included in (2).

### 2.1. Approaches to model subgrid-scale stresses

An eddy-viscosity (EV) closure is typically used to model the SGS tensor. One of the simplest and long-standing nonlinear EV models is the *Smagorinsky model* (Smagorinsky, 1963):

$$\boldsymbol{\tau} = -2(c_s \delta)^2 |\nabla^s \bar{\mathbf{u}}| \nabla^s \bar{\mathbf{u}}, \quad (4)$$

where  $\nabla^s \bar{\mathbf{u}} = \frac{\nabla \bar{\mathbf{u}} + \nabla \bar{\mathbf{u}}^T}{2}$  is the deformation tensor of  $\bar{\mathbf{u}}$ ,  $|\boldsymbol{\mu}| = (2 \mu_{ij} \mu_{ij})^{1/2}$  the norm of any tensor  $\boldsymbol{\mu}$ ,  $c_s$  the Smagorinsky constant.

The main justification for the EV approach is that in homogeneous, isotropic flows, the energy cascading from larger scales through inertial interactions must be dissipated in the mean sense (Frisch et al., 1995; Pope, 2000; Sagaut, 2006; Berselli et al., 2005). There are, however, two potential pitfalls in applying this concept to turbulent stratified flows. The first is that, while energy dissipation holds in the statistical sense, it is not necessarily true instantaneously. Indeed, at particular instances and locations, a significant inverse transfer of energy, called backscatter, from small scales to large scales can take place (Sagaut, 2006). This would thus correspond to a negative viscosity coefficient if represented using EV models. The second fundamental issue is that, unlike in homogenous, isotropic flows, in stratified flows the kinetic energy has dual pathways: it can either be (i) dissipated (energy cascade), or (ii) stored as background potential energy by irreversible mixing (Winters et al., 1995). The proportion of how much kinetic energy is dissipated and how much is converted to background potential energy in various flow configurations is a challenging problem, subject of current research.

In the LES of homogeneous, isotropic flows, the *dynamic* SGS model of Germano et al. (1991) (see also Porté-Agel et al. (2000)) and the *Lagrangian dynamic* SGS model of Meneveau et al. (1996) are considered to be some of the state-of-the-art EV models. In the dynamic SGS model, the constant  $c_s$  is computed dynamically as a function of space and time:

$$c_s^2 = \frac{1}{2} \frac{\langle M_{ij} L_{ij} \rangle}{\langle M_{kl} M_{kl} \rangle}. \quad (5)$$

In (5),  $\langle \cdot \rangle$  denotes spanwise ( $z$ ) averaging, and  $M_{ij}$  and  $L_{ij}$  are defined as follows:

$$M_{ij} = \tilde{\delta}^2 |\nabla^s \tilde{\mathbf{u}}| \nabla^s \tilde{u}_{ij} - \delta^2 |\nabla^s \tilde{\mathbf{u}}| \nabla^s \tilde{u}_{ij} \quad (6)$$

$$= \delta^2 \left( \alpha^2 |\nabla^s \tilde{\mathbf{u}}| \nabla^s \tilde{u}_{ij} - |\nabla^s \tilde{\mathbf{u}}| \nabla^s \tilde{u}_{ij} \right), \quad (7)$$

$$L_{ij} = \tilde{u}_i \tilde{u}_j - \tilde{u}_i \tilde{u}_j, \quad (8)$$

where a tilde denotes filtering with a test filter of radius  $\tilde{\delta}$  and  $\alpha = \frac{\tilde{\delta}}{\delta}$  is the ratio of the radii of the two filters. Defining  $\widehat{M}_{ij} = \frac{M_{ij}}{\delta^2}$ , we can rewrite (5) as

$$c_s^2 = \frac{1}{2} \frac{\langle \widehat{M}_{ij} L_{ij} \rangle}{\langle \widehat{M}_{kl} \widehat{M}_{kl} \rangle}, \quad (9)$$

which depends only on the ratio of filter widths  $\alpha$  and has no explicit dependence on  $\delta$ . While the dynamic method does not preclude computation of negative values of  $c_s$ , we use  $c_s = \max(c_s, 0)$  to ensure numerical stability, as is usually done in practical computations with the dynamic SGS model (Sagaut, 2006). With the spectral element method (Section 3), we project from the  $N$ th-order local basis functions onto a basis of order  $\tilde{N}$ , with corresponding  $\alpha = \frac{N}{\tilde{N}}$ .

A simple approach that is used to incorporate some of the effects of stratification on mixing is to relate diffusivity to the Richardson number  $Ri = N^2 / S^2$ , where  $N^2 = -\frac{g}{\rho_0} \frac{\partial \rho'}{\partial z}$  is the square of the buoyancy frequency, and  $S^2 = \left(\frac{\partial u}{\partial z}\right)^2 + \left(\frac{\partial v}{\partial z}\right)^2$  (Schumann, 1975; Stevens et al., 1998; Dörnbrack, 1998; Özgökmen et al., 2007):

$$\boldsymbol{\sigma} = -g(Ri) (c_T \delta)^2 |\nabla^s \bar{\mathbf{u}}| \nabla^s \bar{\rho}', \quad (10)$$

where

$$g(Ri) = \begin{cases} 1 & \text{for } Ri < 0, \\ \sqrt{1 - \frac{Ri}{Ri_c}} & \text{for } 0 \leq Ri \leq Ri_c, \\ 0 & \text{for } Ri > Ri_c. \end{cases} \quad (11)$$

where  $Ri_c$  is the critical threshold, typically  $Ri_c = 0.25$  (Miles, 1961; Rohr et al., 1988) and  $c_T$  is the counterpart of the Smagorinsky constant for diffusivity. We emphasize that there are several potential problems with this approach. The first is that it is highly empirical and not based on a rigorous derivation. The second issue is that there is growing evidence that there is no definitive  $Ri_c$  beyond which stable stratification overpowers the vertical shear and yield zero mixing. Indeed, mixing may persist for  $Ri \gg Ri_c$ , albeit at much reduced levels (Canuto et al., 2008). Both issues might have significant negative consequences in models where the turbulence closures carry out the entire mixing. In LES, however, the results depend on the complex nonlinear interplay between resolved and parameterized turbulence. Therefore, the model (10) deserves investigation as to whether it can provide a reasonable pathway for enhanced turbulent mixing in the presence of shear.

A completely different approach to represent SGS tensors is provided by so-called *approximate deconvolution* (AD) models (Leonard, 1974; Clark et al., 1979; Carati et al., 2001; Winkelmann et al., 2001; Katopodes et al., 2000; Berselli et al., 2005; John, 2004, 2005; Sagaut, 2006; Cao et al., 2005) that are developed based on mathematical grounds rather than physical insight into the nature of turbulence. A particular version of AD models has been put forward by Galdi et al. (2000) and tested in the numerical simulation of homogenous channel flows (Iliescu and Fischer, 2003, 2004). The so-called *Rational* model is given by:

$$\boldsymbol{\tau} = \left[ \left( -\frac{\delta^2 + \mathbb{I}}{4\gamma} \Delta \right)^{-1} \left( \frac{\delta^2}{2\gamma} \nabla \bar{\mathbf{u}} \nabla \bar{\mathbf{u}} \right) \right], \quad (12)$$

where  $\mathbb{I}$  is the identity operator and  $\gamma$  is the parameter of the Rational model. An improved version of this model was recently tested in stratified flows (Özgökmen et al., 2009). The first modification in (12) was the introduction of a truncated Helmholtz operator. The original version of this operator is computationally expensive and tends to dampen the effect of high wave number features introduced by the nonlinear gradient tensor. The second modification was the derivation of a Rational model for  $\boldsymbol{\sigma}$ :

$$\sigma = \left( -\frac{\delta^2}{4\gamma} \Delta + \mathbb{I} \right)^{-1} \left( \frac{\delta^2}{2\gamma} \nabla \bar{\mathbf{u}} \nabla \bar{\rho}' \right). \quad (13)$$

It should be pointed out that there are other types of EV and AD models that are not tested here. These include high-pass filtered EV models (Stolz et al., 2005) and the AD model which relies on finding an approximate deconvolution of the filtered quantity by repeated filtering (Stolz and Adams, 1999; Schlatter et al., 2004).

## 2.2. SGS models investigated

Given the different classes of approaches discussed above, there are many combinations of SGS models that can be explored. In this study, we investigate the following choices.

The first is the pure dynamic Smagorinsky model, denoted SGS-D here:

$$\tau_{SGS-D} = -2(c_s \delta)^2 |\nabla^s \bar{\mathbf{u}}| \nabla^s \bar{\mathbf{u}} \quad \text{and} \quad \sigma_{SGS-D} = 0, \quad (14)$$

in which  $c_s$  is computed based on the procedure of Germano et al. (1991), and there is no treatment of SGS for the density perturbation. The motivation for employing this model is twofold. First, we investigate how well an approach developed in the context of homogeneous flows would work in LES of stratified flows. Second, it provides a solution with  $\sigma = 0$  so that we can assess the importance of  $\sigma$  models in the outcome of the numerical simulation.

We next investigate the so-called *hybrid* model SGS-H, in which a linear superposition of the dynamic Smagorinsky and Rational models is used in the SGS tensor for momentum:

$$\tau_{SGS-H} = \left( -\frac{\delta^2}{4\gamma} \Delta + \mathbb{I} \right)^{-1} \left( \frac{\delta^2}{2\gamma} \nabla \bar{\mathbf{u}} \nabla \bar{\mathbf{u}} \right) - 2(c_s \delta)^2 |\nabla^s \bar{\mathbf{u}}| \nabla^s \bar{\mathbf{u}} \quad \text{and} \\ \sigma_{SGS-H} = 0. \quad (15)$$

This model combines the ability of the dynamic Smagorinsky model to provide dissipation where and when needed with that of the Rational model for preserving the fine-scale features of the flow field on coarse meshes. SGS-H was found to perform well in our recent study of the lock-exchange problem at a moderate Reynolds number ( $Re = 3000$ , Özgökmen et al. (2009)).

The third SGS model investigated is the Rational model for stratified flows SGS-R:

$$\tau_{SGS-R} = \left( -\frac{\delta^2}{4\gamma} \Delta + \mathbb{I} \right)^{-1} \left( \frac{\delta^2}{2\gamma} \nabla \bar{\mathbf{u}} \nabla \bar{\mathbf{u}} \right) \quad \text{and} \\ \sigma_{SGS-R} = \left( -\frac{\delta^2}{4\gamma} \Delta + \mathbb{I} \right)^{-1} \left( \frac{\delta^2}{2\gamma} \nabla \bar{\mathbf{u}} \nabla \bar{\rho}' \right). \quad (16)$$

Then, we experiment with several mixed models, mainly to explore the possible impact of  $\sigma$  on the accuracy of LES results. Model SGS-E is a combination of the dynamic Smagorinsky model for momentum tensor and *Ri*-dependent Smagorinsky model for density perturbation SGS vector:

$$\tau_{SGS-E} = -2(c_s \delta)^2 |\nabla^s \bar{\mathbf{u}}| \nabla^s \bar{\mathbf{u}} \quad \text{and} \\ \sigma_{SGS-E} = -g(Ri)(c_T \delta)^2 |\nabla^s \bar{\mathbf{u}}| \nabla \bar{\rho}'. \quad (17)$$

In SGS-F, the dynamic SGS model is used for the SGS tensor and the Rational model for the density perturbation SGS vector:

$$\tau_{SGS-F} = -2(c_s \delta)^2 |\nabla^s \bar{\mathbf{u}}| \nabla^s \bar{\mathbf{u}} \quad \text{and} \\ \sigma_{SGS-F} = \left( -\frac{\delta^2}{4\gamma} \Delta + \mathbb{I} \right)^{-1} \left( \frac{\delta^2}{2\gamma} \nabla \bar{\mathbf{u}} \nabla \bar{\rho}' \right). \quad (18)$$

Finally, we add a density perturbation SGS vector to the hybrid model, and denote it SGS-G:

$$\tau_{SGS-G} = \left( -\frac{\delta^2}{4\gamma} \Delta + \mathbb{I} \right)^{-1} \left( \frac{\delta^2}{2\gamma} \nabla \bar{\mathbf{u}} \nabla \bar{\mathbf{u}} \right) - 2(c_s \delta)^2 |\nabla^s \bar{\mathbf{u}}| \nabla^s \bar{\mathbf{u}} \quad \text{and} \quad (19)$$

$$\sigma_{SGS-G} = \left( -\frac{\delta^2}{4\gamma} \Delta + \mathbb{I} \right)^{-1} \left( \frac{\delta^2}{2\gamma} \nabla \bar{\mathbf{u}} \nabla \bar{\rho}' \right). \quad (20)$$

For convenience, these SGS models are summarized in Table 1.

## 3. Numerical model

This numerical study is conducted using Nek5000. This is a code based on the spectral element method (Patera, 1984; Maday and Patera, 1989; Fischer, 1997). We note that similar spectral element discretizations have been used in other DNS studies of the lock-exchange problem (Cantero et al., 2007; Härtel et al., 2000). Nek5000 has been already used in the numerical investigation of various LES models in homogeneous flows (Iliescu and Fischer, 2003, 2004), stratified flows (Özgökmen et al., 2007, 2009), and bottom gravity currents (Özgökmen et al., 2004a,b, 2006; Özgökmen and Fischer, 2008). These results have formed the basis of refined parameterizations of gravity current mixing for an ocean general circulation model (Chang et al., 2005; Xu et al., 2006).

The time advancement of the Boussinesq equations (1) is based on second-order semi-implicit operator-splitting methods (Maday et al., 1990; Fischer, 1997). The hydrodynamics are advanced first, with explicit treatment of the buoyancy forcing term, followed by the update of the density perturbation transport. Spatial discretization is based on the spectral element method, which is a high-order weighted residual technique based on compatible velocity and pressure spaces free of spurious modes. Locally, the spectral element mesh is structured, with the solution, data, and geometry expressed as sums of *N*th-order Lagrange polynomials on tensor-products of Gauss–Lobatto–Legendre (GLL) quadrature points. Globally, the mesh is an unstructured array of *K* deformed hexahedral elements and can include geometrically nonconforming elements. For problems having smooth solutions, the spectral element method achieves exponential convergence with *N*, despite having only  $C^0$  continuity (which is advantageous for parallelism). The convection operator exhibits minimal numerical dissipation and dispersion, which is critical for high Reynolds number applications. For the sparse linear solvers, Nek5000 employs as a preconditioner the additive overlapping Schwarz method (Dryja and Widlund, 1987; Fischer and Ronquist, 1994; Fischer, 1997; Fischer and Gottlieb, 1997; Lottes and Fischer, 2005), which uses fast local solvers that exploit the tensor-product form and a parallel coarse-grid solver that scales to thousands of processors (Tufo and Fischer, 2001).

The nonlinear advection term in the momentum equation of (1) generates energy at high wave numbers that cannot be captured on the mesh. This can lead to an accumulation of energy at smaller scales. Two methods are employed in Nek5000 that help achieve numerical stability at high *Re* without compromising the solution accuracy. The first method is dealiasing through the 3/2 rule (Deville et al., 2002). The second method, first proposed by Fischer and Mullen (2001), is polynomial filtering, in which the coefficient of the highest order basis polynomial is reduced by a  $\beta$  fraction. This will dampen high-frequency oscillations and reduce the accumulation of energy in the highest wave numbers. In the present study, all computations are carried out with dealiasing and 5% polynomial filtering ( $\beta = 0.05$ ).

We should emphasize that, in our numerical study, the effect of polynomial filtering is entirely decoupled from the effect of LES modeling. Indeed, in all our numerical tests, when we compared under-resolved simulations (DNS') with LES, we always used the same spatial resolution, the same temporal resolution, and the

**Table 1**  
List of the SGS models investigated in this study.

Dynamic Smagorinsky model SGS-D	$\tau_{SGS-D} = -2 (c_s \delta)^2  \nabla^s \mathbf{u}  \nabla^s \mathbf{u}$ $\sigma_{SGS-D} = 0$
Hybrid model SGS-H	$\tau_{SGS-H} = \left( -\frac{\delta^2}{4\gamma} \Delta + \mathbb{I} \right)^{-1} \left( \frac{\delta^2}{2\gamma} \nabla \mathbf{u} \nabla \mathbf{u} \right) - 2 (c_s \delta)^2  \nabla^s \mathbf{u}  \nabla^s \mathbf{u}$ $\sigma_{SGS-H} = 0$
Rational model SGS-R	$\tau_{SGS-R} = \left( -\frac{\delta^2}{4\gamma} \Delta + \mathbb{I} \right)^{-1} \left( \frac{\delta^2}{2\gamma} \nabla \mathbf{u} \nabla \mathbf{u} \right)$ $\sigma_{SGS-R} = \left( -\frac{\delta^2}{4\gamma} \Delta + \mathbb{I} \right)^{-1} \left( \frac{\delta^2}{2\gamma} \nabla \mathbf{u} \nabla \rho' \right)$
Mixed model SGS-E	$\tau_{SGS-E} = -2 (c_s \delta)^2  \nabla^s \mathbf{u}  \nabla^s \mathbf{u}$ $\sigma_{SGS-E} = -g(Ri) (c_T \delta)^2  \nabla^s \mathbf{u}  \nabla \rho'$ <p>where <math>g(Ri)</math> is given in (11)</p>
Mixed model SGS-F	$\tau_{SGS-F} = -2 (c_s \delta)^2  \nabla^s \mathbf{u}  \nabla^s \mathbf{u}$ $\sigma_{SGS-F} = \left( -\frac{\delta^2}{4\gamma} \Delta + \mathbb{I} \right)^{-1} \left( \frac{\delta^2}{2\gamma} \nabla \mathbf{u} \nabla \rho' \right)$
Mixed model SGS-G	$\tau_{SGS-G} = \left( -\frac{\delta^2}{4\gamma} \Delta + \mathbb{I} \right)^{-1} \left( \frac{\delta^2}{2\gamma} \nabla \mathbf{u} \nabla \mathbf{u} \right) - 2 (c_s \delta)^2  \nabla^s \mathbf{u}  \nabla^s \mathbf{u}$ $\sigma_{SGS-G} = \left( -\frac{\delta^2}{4\gamma} \Delta + \mathbb{I} \right)^{-1} \left( \frac{\delta^2}{2\gamma} \nabla \mathbf{u} \nabla \rho' \right)$

same level of polynomial filtering. Thus, the improvement of the LES results over the DNS<sup>\*</sup> results is entirely due to the SGS terms, and not to the polynomial filtering.

#### 4. Model configuration and parameters

The model setup is similar to that in Özgökmen et al. (2009), which contains a detailed discussion of the boundary conditions, initial conditions and parameters used. In this section, we mainly highlight the differences.

The computational domain is  $-\frac{1}{2} \leq x \leq \frac{1}{2}$ ,  $0 \leq y \leq W$ , and  $0 \leq z \leq H$ , where  $L/H = 2$  and  $W/H = 1$ . The aspect ratio  $L/H$  appears to be an important parameter of the system; in long domains,  $L \gg H$ , the dynamics consist of essentially two-layer exchange flow, where the shear between the counter-propagating gravity currents leads to the formation of Kelvin–Helmholtz rolls, and the mixing takes place by the stirring in these rolls towards smaller scale filaments and their turbulent breakdown by secondary instabilities. As such, a domain with  $L \gg H$  has mainly stably-stratified turbulent mixing. Such a system was studied in some detail recently by Ilicak et al. (2009). On the other hand, in a short domain,  $L \ll H$ , the gravity currents encounter with and move along the vertical walls, until gravitational force overpowers the inertia and an oscillatory motion sets in. In this case, convective motions are quite important. A domain with  $L \approx H$  appears to have two advantages. First, it contains both stably-stratified overturns and convective motions with a rapid transition between them. Therefore, the flow field is quite complex and poses a demanding test for SGS models. Second, the domain is smaller than the case with  $L \gg H$ , which has significant computational advantages in terms of the spatial resolution.

Next, we discuss the selection of the non-dimensional parameters in (2). The Froude number  $Fr$  is the ratio between the characteristic advection speed and the internal wave speed. Given that the system starts as a counter-propagating gravity current prob-

lem, these two speeds are related and one should select a  $Fr$  consistently. In this problem, the initial vertical scale of the gravity currents is  $\ell \approx H/2$  and  $U_0 \approx \sqrt{g \Delta \rho' \ell (H - \ell) / (\rho_0 H)} \approx \frac{1}{2} \sqrt{g \Delta \rho' H / \rho_0}$ . Therefore, the Froude number is set to  $Fr = 2^{-\frac{1}{2}}$ . The Peclet number can be written as  $Pe = Re Pr$ , where  $Pr = \nu / \kappa$  is the Prandtl number. Corresponding to that of heat and water in room temperature, we take  $Pr = 7$ . In a system of salt water, which is also of oceanic interest,  $Pr \approx 700$ , indicating that mixing takes place at much finer scales. Such a system is far more computationally challenging than the present one, and will be investigated in a future study. The only remaining physical parameter of the problem is  $Re$ , which controls the range of turbulent features and interactions in the flow field, and as such, is of great interest. Here, we conduct well-resolved simulations at four Reynolds numbers, namely  $Re = 10^3$ ,  $Re = 3 \times 10^3$ ,  $Re = 10^4$  and  $Re = 3 \times 10^4$ . We start from  $Re = 10^3$ , because at smaller  $Re$  the system displays only reduced turbulent features. Because of the heavy burden posed by DNS on both storage and CPU time, with the available computational resources we can only achieve  $Re = 3 \times 10^4$ . Using DNS as ground truth, various SGS models introduced in Section 2.2 are tested. We subsequently explore  $Re = 10^5$  and  $Re = 10^6$  using LES.

Numerical experiments are carried out at nine different resolutions (Table 2), the purpose of which is twofold. The first is to achieve results that are approximately independent of the spatial resolution so that they can serve as ground truth (DNS). The second is to identify those coarse resolutions that result into significant differences with respect to DNS and can be potentially improved using SGS models. We start with  $K_x = 16$ ,  $K_y = 8$ ,  $K_z = 8$  equally-spaced elements in  $x, y, z$  directions, respectively, and a polynomial order  $N = 6$  (corresponding to a number of grid points of  $n = (K_x N + 1)(K_y N + 1)(K_z N + 1) = 232,897$ ). This resolution is denoted low-res1. The spectral element formulation provides dual pathways for convergence (linear with increasing  $K$  and exponential with  $N$ ) and we employ both. In low-res2, the polynomial order is increased to

$N = 8$  ( $n = 545, 025$ ). Then, the number of elements is doubled in each direction,  $K_x = 32, K_y = 16, K_z = 16$  (mid-res1,  $n = 4, 276, 737$ ), and the polynomial order is gradually increased to  $N = 10$  (mid-res2,  $n = 8, 320, 614$ ),  $N = 12$  (mid-res3,  $n = 14, 340, 865$ ),  $N = 15$  (high-res1,  $n = 27, 939, 961$ ), and  $N = 17$  (high-res2,  $n = 40, 618, 305$ ). The number of elements is then increased to  $K_x = 48, K_y = 24, K_z = 24$ , while the polynomial order is set to  $N = 14$  (high-res3,  $n = 61, 230, 625$ ). Finally, the polynomial order is increased to  $N = 15$  for high-res4 with  $n = 76, 431, 937$ . The spatial resolutions used in the experiments are shown as a function of  $Re$  in Table 3.

Given the available computational resources, we can only run multiple numerical experiments at high spatial resolutions (such as high-res4) provided that the total number of time steps is kept to a minimum. Therefore, the total integration time  $T$  (or non-dimensional  $T^*$ ) is determined as follows. The time needed for the gravity currents to cross the domain is  $T_p = L/U_0$ . Thus,  $T/T_p = T^*/4$ . Another inherent time scale of interest is the buoyancy period  $T_b = 2\pi N_\infty^{-1}$ , where  $N_\infty = \sqrt{\frac{g}{\rho_0} \frac{\Delta\rho'}{H}}$  is the buoyancy frequency based on the density difference over the total vertical extent  $H$  of the system. We get  $T/T_b = T^*/(2\pi)$ . The simulations are integrated until a non-dimensional time of  $T^* = 13.5$ , which corresponds to  $T^*/T_p = 3.35$  and  $T^*/T_b = 2.15$ . The integration time is adequate for multiple sloshings, for the bulk of the turbulent mixing to take place, and for differences among numerical experiments to become apparent. It is, however, shorter than the time needed to achieve a state of rest. This is a compromise that we made in order to carry out numerical simulations for the entire range of parameters ( $Re$ , SGS models) with the available computational resources. Results from a total of 50 numerical experiments are described here. The computation times for the numerical experiments are listed in Table 2. The computation (CPU) time is approximately proportional to  $mKN^4$ , where  $m$  is the number of time steps (needed to reach non-dimensional time  $t^* = 13.5$ ). Most experiments are completed on University of Miami's Linux cluster based on 2.3 GHz Xeon CPUs and gigabit interconnect. Some of the experiments are run on Virginia Tech's SystemX, based on 2200 Apple G5 processors with 2.3 GHz and InfiniBand interconnect. SystemX can be up to 1.6 times faster than the University of Miami's cluster.

**Table 2**

Table of the spatial resolutions used for the numerical simulations. Approximate CPU times are listed for DNS and DNS\*. Wall-clock time is CPU hours divided by the number of processors  $P$ . The symbol “⊗” differentiates the computations on SystemX from those on the University of Miami's cluster.

Exp	Resolution	$m$	$P$	CPU hours
low-res1	$K = 16 \times 8 \times 8 = 1024; N = 6$ $n = 232, 897$	15,000	8–32	24
low-res2	$K = 16 \times 8 \times 8 = 1024; N = 8$ $n = 545, 025$	15,000	8–32	77
mid-res1	$K = 32 \times 16 \times 16 = 8192; N = 8$ $n = 4, 276, 737$	15,000	64–128	1130
mid-res2	$K = 32 \times 16 \times 16 = 8192; N = 10$ $n = 8, 320, 641$	23,000	64–128	4100
mid-res3	$K = 32 \times 16 \times 16 = 8192; N = 12$ $n = 14, 340, 865$	30,000	96–256	9000
high-res1	$K = 32 \times 16 \times 16 = 8192; N = 15$ $n = 27, 939, 961$	40,000	128	18,000
high-res2	$K = 32 \times 16 \times 16 = 8192; N = 17$ $n = 40, 618, 305$	58,000	128	49,000
high-res3	$K = 48 \times 24 \times 24 = 27, 648; N = 13$ $n = 61, 230, 625$	55,000	192	25,344 <sup>⊗</sup>
high-res4	$K = 48 \times 24 \times 24 = 27, 648; N = 14$ $n = 76, 431, 937$	55,000	192	36,480 <sup>⊗</sup>

The accuracy of the SGS models is evaluated through *a posteriori* testing. The main measure used is the background/reference potential energy (RPE), which exactly quantifies mixing in an enclosed system (Winters et al., 1995). RPE is the minimum potential energy that can be obtained through an adiabatic redistribution of the water masses. To compute RPE, we use the probability density function approach introduced by Tseng and Ferziger (2001). Specifically, we split the density perturbation field into 51 bins at each time step, and integrate:

$$RPE = gLW \int_0^H \rho'(z_r) z_r dz_r, \quad (21)$$

where  $z_r(\rho')$  is the height of fluid of density  $\rho'$  in the minimum potential energy state. It is convenient to use the non-dimensional background potential energy

$$RPE^*(t^*) \equiv \frac{RPE(t^*) - RPE(0)}{RPE(0)}, \quad (22)$$

which shows the relative increase of the RPE with respect to the initial state by mixing. Further discussion of the energetics of the lock-exchange problem can be found in Özgökmen et al. (2007, 2009).

Finally, the parameters of the SGS models are listed in Table 4. These values are chosen based on the parameter study conducted in Özgökmen et al. (2009).

## 5. Results

The results are organized as follows. First, we present DNS and DNS\*, which are used to establish the ground truth for mixing at different  $Re$  and spatial resolutions suitable for LES, respectively. Then, we test the various SGS models listed in Table 1 at different  $Re$ . Specifically, we compare the mixing curves  $RPE^*(t^*)$  for these LES models to those from DNS. Finally, we carry out LES at  $Re$  for which a DNS is not feasible with our available computational resources.

### 5.1. Direct numerical simulations for $10^3 \leq Re \leq 3 \times 10^4$

Since the density perturbation field is an active tracer, it provides a convenient way to visualize turbulent flows. The wave number spectra of kinetic energy are another commonly used tool in the numerical investigation of turbulent flows. Finally, the normalized background potential energy is an accurate measure for quantifying mixing in an enclosed domain. We will use all three criteria to assess the changes in the flow when  $Re$  is changed.

The system starts from rest. It is initialized with colder water on the left and warmer water on the right of the domain, separated by a sharp interface with a sinusoidal perturbation that is intended to facilitate transition to 3D flow (Fig. 1a). By the time the counter-propagating gravity currents reach the side walls ( $t^* \approx 1.75$ ), the case with  $Re = 10^3$  shows hints of two Kelvin–Helmholtz (KH) rolls (Fig. 1b). At a later time ( $t^* = 4.8$ , Fig. 1c), the overturning eddies

**Table 3**

Table of the spatial resolutions used as a function of the  $Re$ .

Resolution	$Re = 10^3$	$Re = 3 \times 10^3$	$Re = 10^4$	$Re = 3 \times 10^4$
low-res1 $n = 232, 897$	DNS*	DNS*	DNS*	DNS*
low-res2 $n = 545, 025$	DNS	DNS*	DNS*	DNS*
mid-res1 $n = 4, 276, 737$	DNS	DNS*	DNS*	–
mid-res2 $n = 8, 320, 641$	DNS	DNS*	–	–
mid-res3 $n = 14, 340, 865$	–	DNS	DNS*	DNS*
high-res1 $n = 27, 939, 961$	–	–	DNS*	DNS*
high-res2 $n = 40, 618, 305$	–	–	DNS	–
high-res3 $n = 61, 230, 625$	–	–	–	DNS*
high-res4 $n = 76, 431, 937$	–	–	–	DNS*

**Table 4**  
Parameters of the LES models used in this study.

SGS-D	$\alpha = N/(N - 1)$ and $\alpha = N/(N - 2)$ or $\alpha = 1.2$ and $\alpha = 1.5$
SGS-H	$\alpha = N/(N - 1), \gamma = 3$
SGS-R	$\gamma = 3, \gamma_T = 15$
SGS-E	$\alpha = N/(N - 1), c_T = 0.03, Ri_c = 0.25$
SGS-F	$\alpha = N/(N - 1), \gamma_T = 15$
SGS-G	$\alpha = N/(N - 1), \gamma = 3, \gamma_T = 15$

appear to carry out the stirring of the density perturbation field and the KH rolls are susceptible to a secondary instability, whereby the stream-wise vortices stretch and tilt the spanwise vorticity concentrated in KH rolls (Klaassen and Peltier, 1989, 1991). Nevertheless, the flow field is not very turbulent at this  $Re$ . At the end of the integration period ( $t^* = 13.5$ ), the density interface becomes smoother due to the decrease of the shear leading to the turbulent interactions, while the density interface thickens due to mixing.

During the initial phase ( $t^* = 1.75$ ), as the  $Re$  is increased, one observes more defined Kelvin–Helmholtz rolls at  $Re = 3 \times 10^3$  (Fig. 2a), more rapid development of the 3D flow structure at  $Re = 10^4$  (Fig. 2b) and complex turbulent coherent structures at  $Re = 3 \times 10^4$  (Fig. 2c). At a later stage coinciding with the period of intense turbulent mixing ( $t^* = 4.8$ ), individual filaments and

structures such as hair-pin vortices are still visible in the density perturbation field at  $Re = 3 \times 10^3$  (Fig. 3a). At  $Re = 10^4$  and  $Re = 3 \times 10^4$ , we notice the appearance of fully-developed turbulence.

The wave number spectra of the kinetic energy  $KE = \frac{1}{2}(u^2 + v^2 + w^2)$  are computed based on 121 spanwise cross-sections taken in the middle of the domain (at  $x = 1$  and  $y = 0.5$ ) at  $t^* = 4.8$  (Fig. 3). The results shown in Fig. 4 indicate that the width of the inertial range where  $E(k) \sim k^{-5/3}$  has the following behavior when  $Re$  is increased: It increases for  $Re \geq 3 \times 10^3$ , is minimal for  $Re = 3 \times 10^3$ , and is fairly well-established for  $Re = 3 \times 10^4$ . When  $Re = 10^3$ , the kinetic energy spectrum  $E(k)$  shows a steeper decay and a narrower spectrum than the others.

Fig. 5 presents the time evolution of the background potential energy  $RPE^*(t^*)$  for  $Re = 10^3$  at all the spatial resolutions listed in Table 3. During the integration period,  $RPE^*(t^*)$  increases monotonically due to irreversible mixing. The maximum value reached is  $RPE^*(t^* = 13.5) \approx 0.097$  for low-res1 and  $RPE^*(t^* = 13.5) \approx 0.105$  for low-res2, mid-res1 and mid-res2. The curves from the latter three spatial resolutions collapse, which is a clear indication of numerical convergence for the  $RPE^*$  metric. Therefore, these curves are considered as DNS. The result from low-res1 seems to slightly overestimate the mixing. We denote it as DNS\*. Overall, the case with  $Re = 10^3$  seems not to pose a challenge, probably because of the lack of intense turbulence (Figs. 1 and 4). Thus, given only a very small discrepancy between low-res1 DNS\* and DNS, we will not investigate LES at  $Re = 10^3$ .

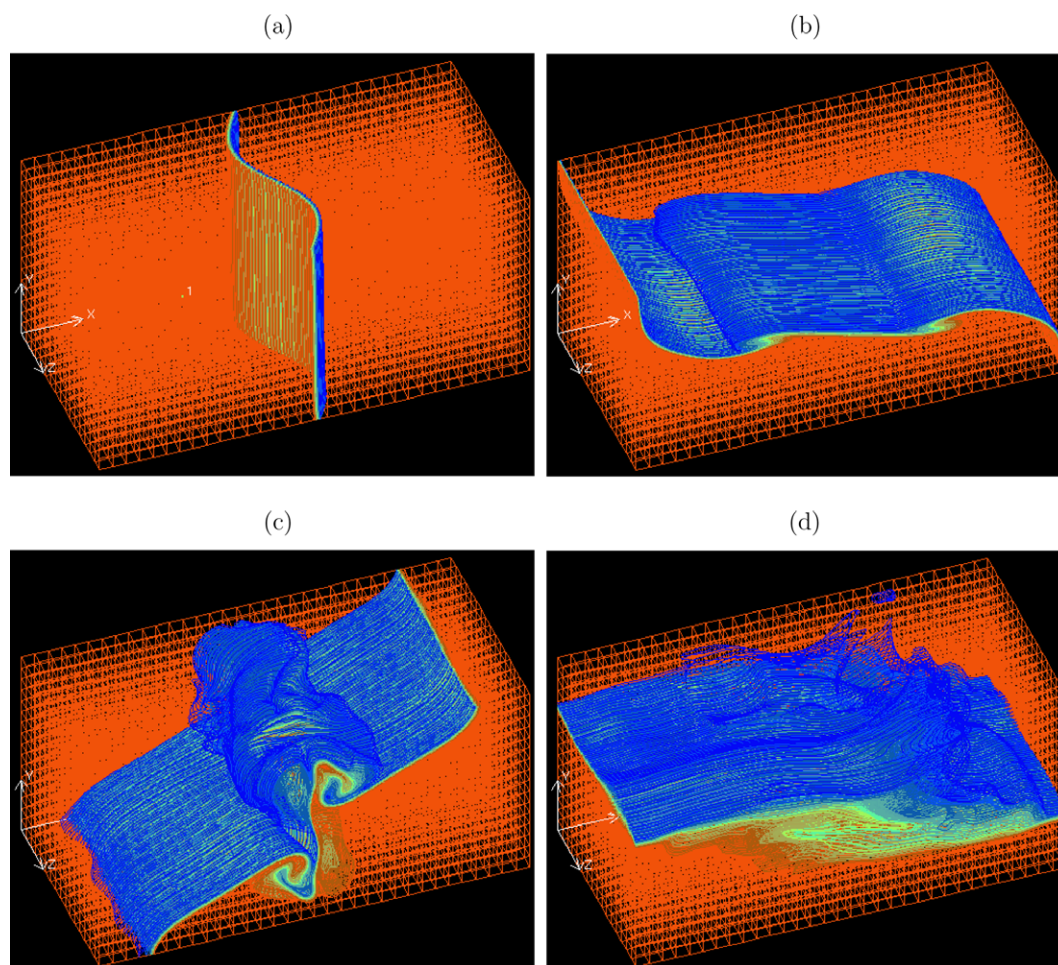


**Fig. 1.** Distribution of the density perturbation  $\rho'(x, y, z, t)/\rho_0$  for  $Re = 10^3$  at mid-res2 resolution (a) at the initial time  $t^* = 0$ , (b) just before the first interaction with the side walls  $t^* = 1.75$ , (c) at an intermediate time  $t^* = 4.8$ , and (d) at the end of the simulation.

Results for  $Re = 3 \times 10^3$  appear to be more challenging (Fig. 6). Indeed, the  $RPE^*$  curve corresponding to low-res1 clearly deviates from the others and overestimates the DNS  $RPE^*$  by up to 50%. There is good agreement among the other  $RPE^*$  curves, but small differences do exist. Thus, we conducted simulations at mid-res3 to ensure that we achieved numerical convergence (DNS). Fig. 6 clearly indicates that SGS models used at low-res1 could possibly rectify the DNS divergence from the truth for  $t^* > 9$ .

As the  $Re$  increases even further, convergence of the  $RPE^*$  curves becomes more challenging. Of course, the net effect of a higher  $Re$  is an increase in the number of spatial points needed to adequately capture the dynamics. Results with  $Re = 10^4$  are shown in Fig. 7. There is a good agreement between computations with high-res1 and high-res2. The discrepancy between these two simulations is small and only appears during intervals of  $4 \leq t^* \leq 6$  and  $12 \leq t^* \leq 13.5$ . This corresponds to the period when the tilting density interface crosses the spanwise edges of the domain. Given their computational cost, a higher resolution case is not deemed necessary. Thus, high-res2 is denoted as DNS. There are significant differences between the  $RPE^*$  curve for high-res2 and the  $RPE^*$  curve for low-res2 to mid-res3. These differences, however, remain smaller than  $\approx 15\%$ . The coarser resolution case low-res1 DNS clearly deviates from the others significantly and indicates excessive mixing at all times.

Finally, results from  $Re = 3 \times 10^4$  are shown in Fig. 8. For this relatively high  $Re$ , we resorted to the largest computations we can currently carry out with the available resources at University of Miami and Virginia Tech. We found that results from mid-res3,

high-res1, high-res3 and high-res4 DNS initially show approximately the same mixing pathway, but then start to diverge. Overall, we are unable to claim to have achieved DNS in this case. Thus, the results from high-res4 DNS represent our best estimate of mixing at  $Re = 3 \times 10^4$ . As before, coarser resolution cases with low-res1 and low-res2 deviate rather significantly from high-res4 DNS. In light of the above discussion, in Sections 5.2 and 5.3 we choose the resolution low-res1 to test the SGS models at all three  $Re$ .

The time evolutions of the background potential energy  $RPE^*(t^*)$  from DNS with different  $Re$  are compared in Fig. 9. There is no significant difference in mixing between the cases with  $Re = 10^3$  and  $Re = 3 \times 10^3$ . The latter shows that the rate of mixing slows down for  $6 \leq t^* \leq 8$ , when the density interface first comes to a standstill and then the direction of tilting is reversed by the gravitational force. We also notice that, at all times, there is a significant jump in the rate of mixing for  $Re = 10^4$  with respect to those from  $Re = 10^3$  and  $Re = 3 \times 10^3$ . At the end of the simulations, we find that  $RPE^*(t^* = 13.5) \approx 0.097$  for  $Re = 10^3$  and  $Re = 3 \times 10^3$ ,  $RPE^*(t^* = 13.5) \approx 0.131$  for  $Re = 10^4$ , and  $RPE^*(t^* = 13.5) \approx 0.144$  for  $Re = 3 \times 10^4$ . Given the computational expense of the high-res4 DNS needed for  $Re = 3 \times 10^4$ , we next explore the accuracy of various SGS in order to attain estimates of mixing at higher  $Re$ .

### 5.2. Large eddy simulations for $3 \times 10^3 \leq Re \leq 3 \times 10^4$

Since in the case with  $Re = 10^3$  fairly good results are achieved at marginal resolutions and computational cost, LES is not deemed

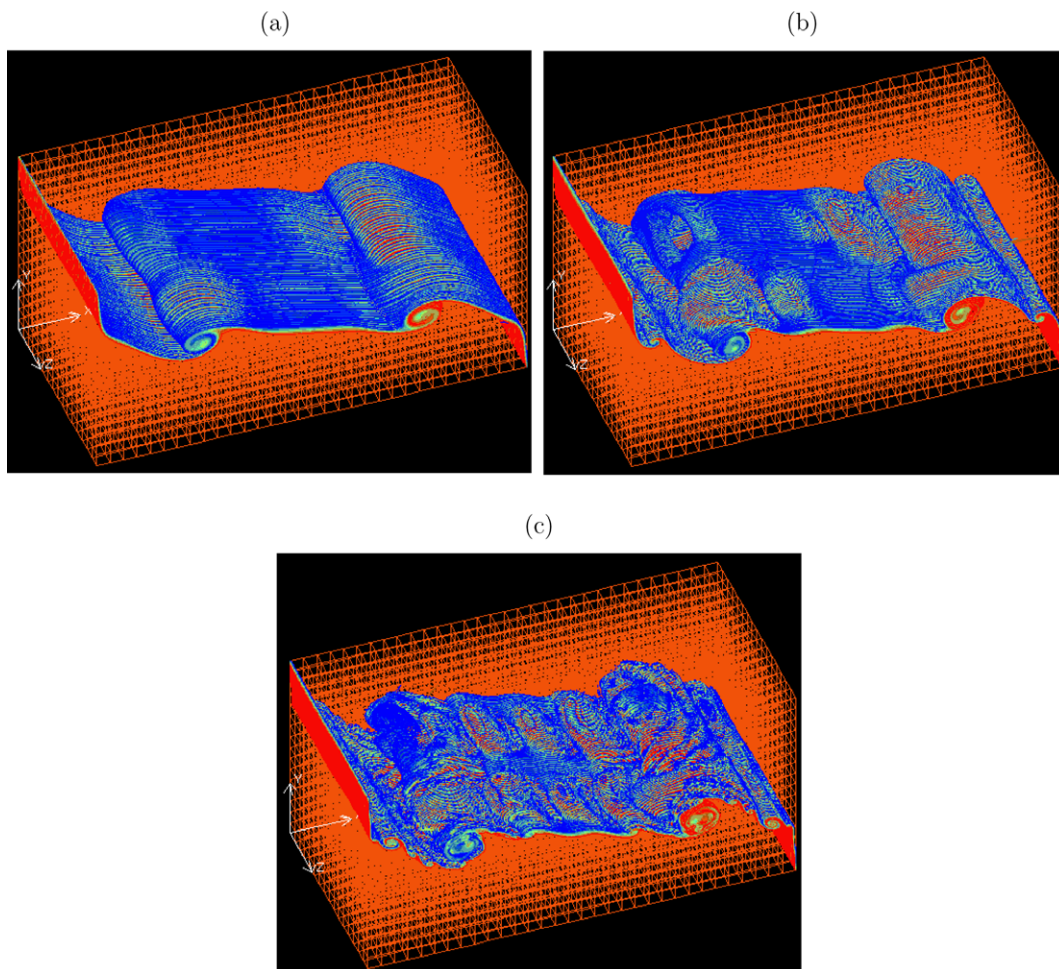


**Fig. 2.** Distribution of the density perturbation  $p'(x, y, z, t)/\rho_0$  at  $t^* = 1.75$  for (a)  $Re = 3 \times 10^3$  at mid-res3 resolution, (b)  $Re = 10^4$  at high-res2 resolution, and (c)  $Re = 3 \times 10^4$  at high-res1 resolution. The animation of the last simulation can be downloaded from: <http://www.rsmas.miami.edu/personal/tamay/3D/dbRe30k.gif>.

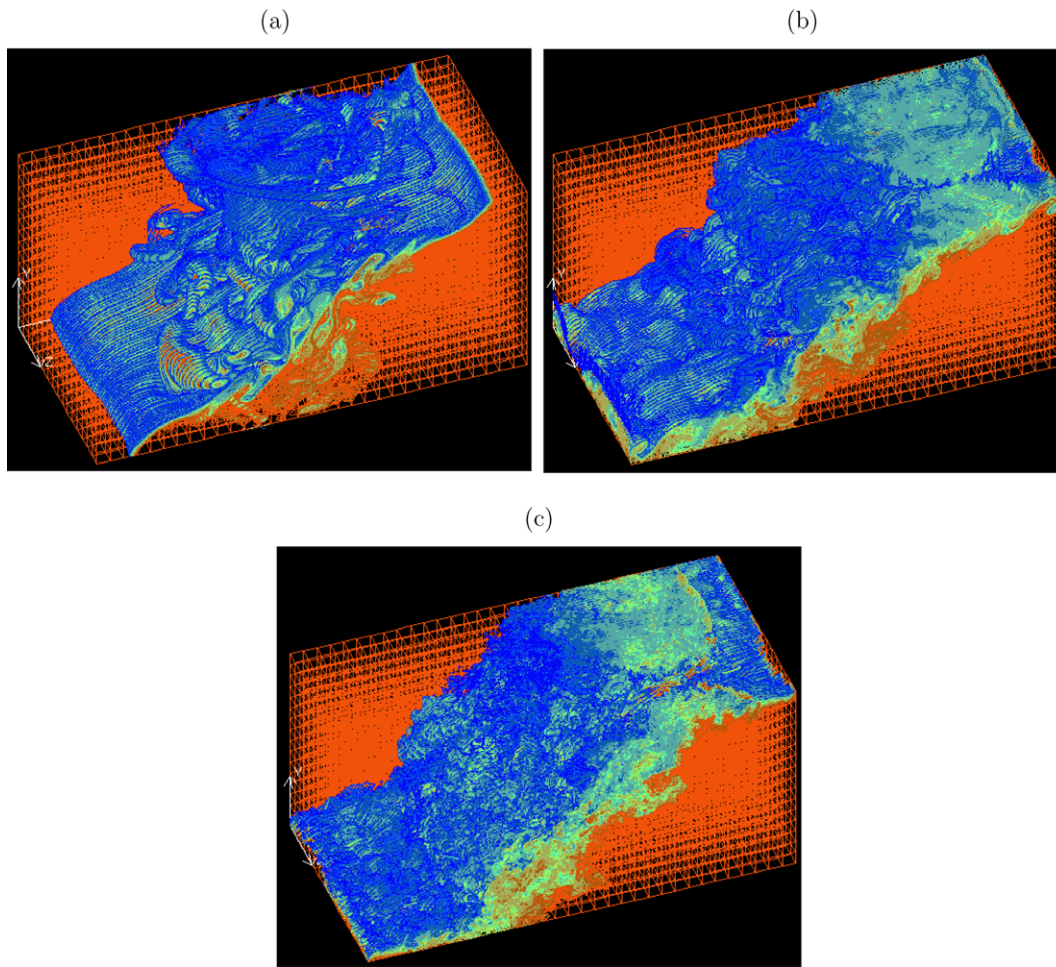


Fig. 3. Same as in Fig. 2, but for  $t^* = 4.8$ .

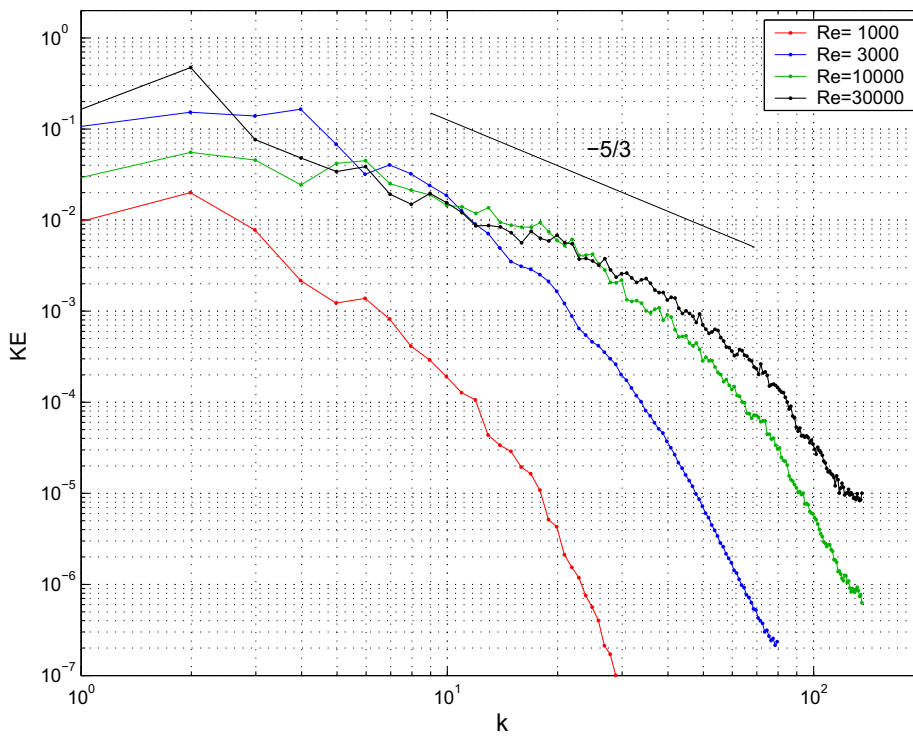


Fig. 4. Wave number spectra of kinetic energy from direct numerical simulations at  $Re = 10^3$ ,  $Re = 3 \times 10^3$ ,  $Re = 10^4$  and  $Re = 3 \times 10^4$ .

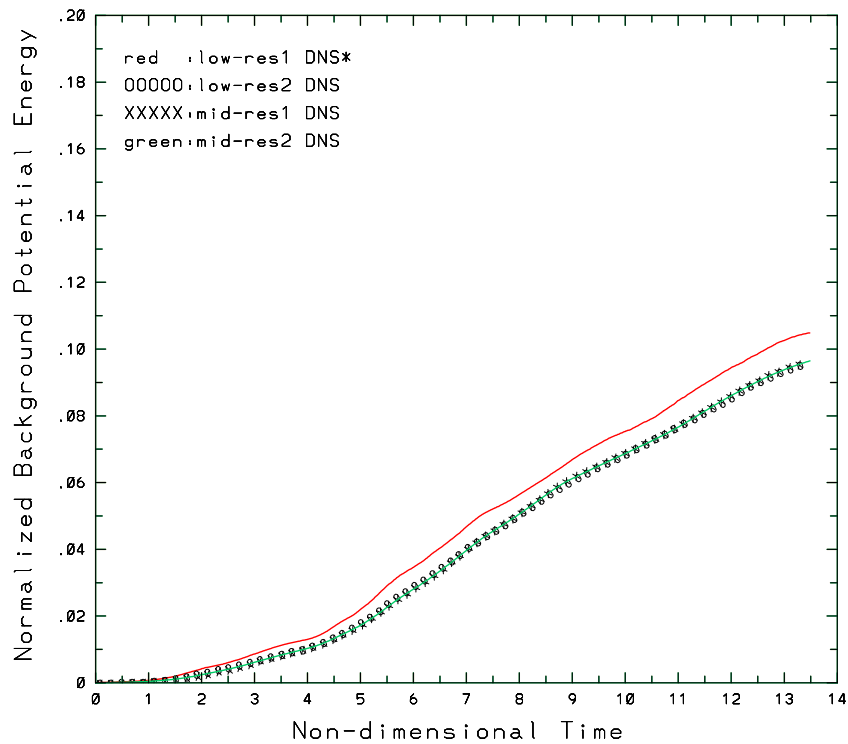


Fig. 5. Time evolutions of the normalized background potential energy  $RPE^*(t^*)$  from DNS<sup>\*</sup> with  $Re = 10^3$  and different resolutions.

appropriate. Indeed, for this  $Re$ , LES would yield the same qualitative results as DNS<sup>\*</sup> at a higher computational cost. For higher  $Re$ , however, DNS<sup>\*</sup> cannot provide accurate results, and thus LES is employed instead. For  $Re = 3 \times 10^3$  and  $Re = 10^4$ , we use the DNS results from Section 5.1 as benchmarks (truth solutions). For

$Re = 3 \times 10^4$ , we do not have a DNS available. Thus, for this  $Re$ , we will use as benchmark the results for the highest resolution achieved. LES at  $Re = 3 \times 10^3$ ,  $Re = 10^4$  and  $Re = 3 \times 10^4$  are conducted using the coarsest mesh, low-res1. To decouple the numerical effects from the LES modeling effects, we also use low-res1 DNS<sup>\*</sup>.

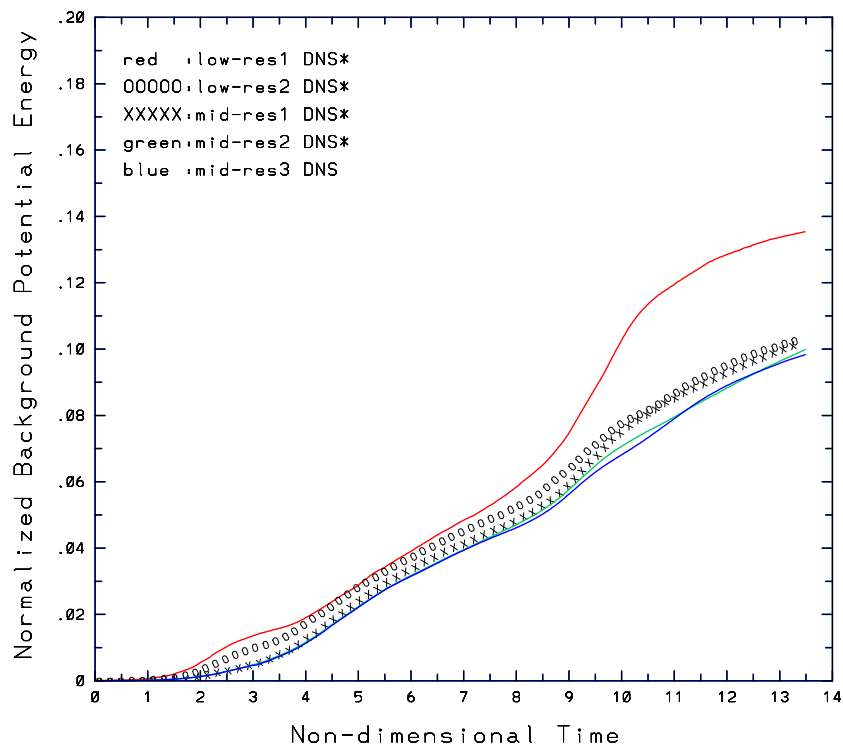


Fig. 6. Time evolutions of the normalized background potential energy  $RPE^*(t^*)$  from DNS<sup>\*</sup> with  $Re = 3 \times 10^3$  and different resolutions.

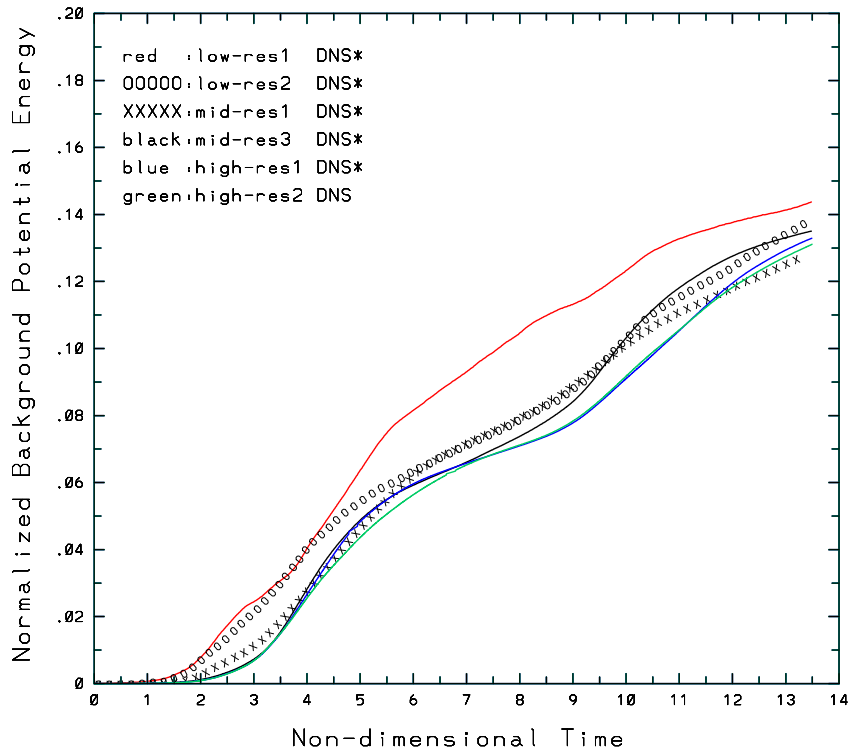


Fig. 7. Time evolutions of the normalized background potential energy  $RPE^*(t^*)$  from DNS<sup>\*</sup> with  $Re = 10^4$  and different resolutions.

The primary measure of success in the SGS modeling is the following: First, the low-res1 LES must yield better results than low-res1 DNS<sup>\*</sup>. Then, the closer the LES results are to the DNS results, the better the SGS model. We define the following metric, which quantifies the rms error of the time evolution of background potential energy in LES with respect to DNS, normalized by the rms error between DNS<sup>\*</sup> and DNS:

$$\eta \equiv \frac{\sqrt{\frac{1}{T^*} \int_{t^*=0}^{t^*=T^*} (RPE_{LES}^*(t^*) - RPE_{DNS}^*(t^*))^2}}{\sqrt{\frac{1}{T^*} \int_{t^*=0}^{t^*=T^*} (RPE_{DNS^*}^*(t^*) - RPE_{DNS}^*(t^*))^2}} \quad (23)$$

Another important consideration for LES is the computational expense of various SGS models, but this was discussed in detail in Özgökmen et al. (2009). The compute times of all LES runs are

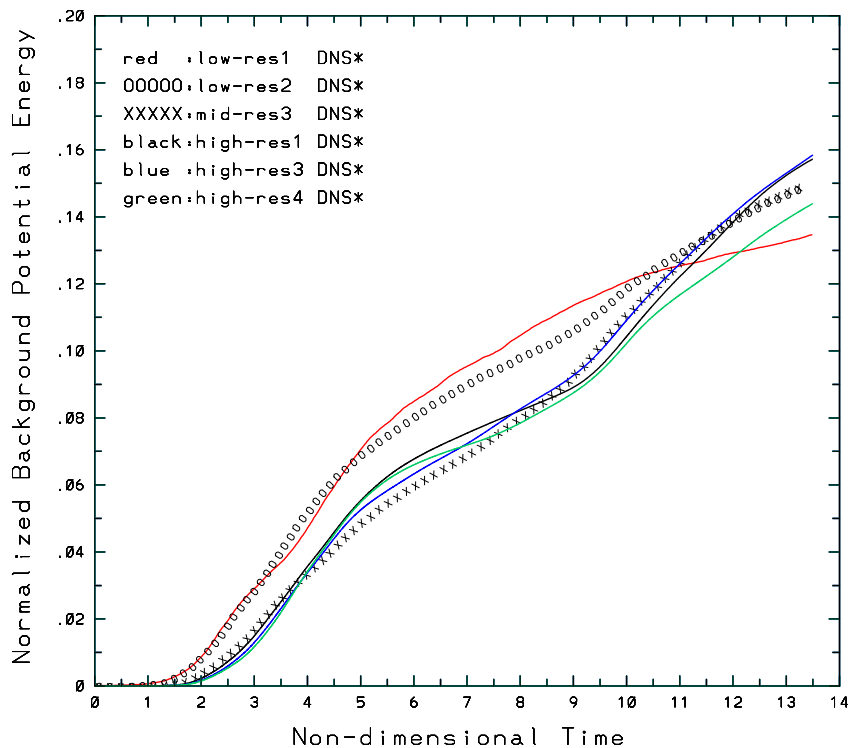


Fig. 8. Time evolutions of the normalized background potential energy  $RPE^*(t^*)$  from DNS<sup>\*</sup> with  $Re = 3 \times 10^4$  and different resolutions.

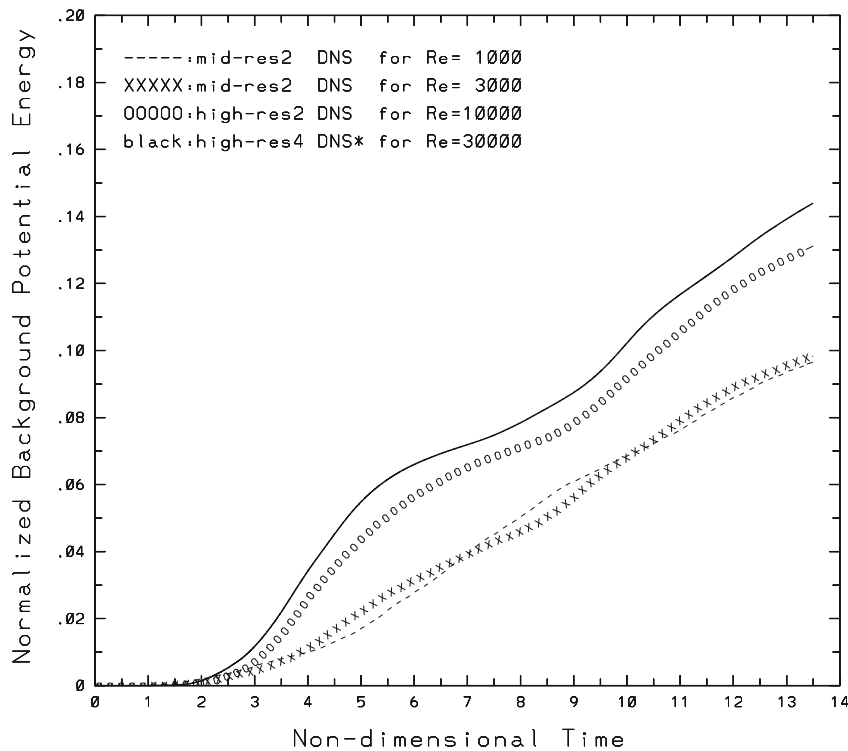


Fig. 9. Comparison of the time evolutions of normalized background potential energy  $RPE^*(t^*)$  from DNS with different  $Re$ .

within a factor of two of the equivalent resolution DNS<sup>\*</sup> listed in Table 2, and offer a drastic reduction in computational cost with respect to DNS (up to 2000-fold reduction in CPU time).

For each  $Re$ , we present 7 LES simulations (Table 1); one for each SGS model, namely SGS-H, SGS-R, SGS-E, SGS-F, SGS-G, and two with SGS-D in order to test the sensitivity to the parameter  $\alpha$  (Table 4).

Results at  $Re = 3 \times 10^3$  are shown in Fig. 10. LES with SGS-H, SGS-R, SGS-G and SGS-D ( $\alpha = 1.5$ ) lead to significant improvements with respect to DNS<sup>\*</sup>, while SGS-E, SGS-F and SGS-D with  $\alpha = 1.2$  show no major change. At  $Re = 10^4$  (Fig. 11), all models show consistent results with DNS, except SGS-D with  $\alpha = 1.5$  and SGS-H. Finally, for  $Re = 3 \times 10^4$  (Fig. 12), all models do a better job than DNS<sup>\*</sup> up to  $t^* \approx 10$ , when some LES models fail to match the increasing rate of mixing of the high-res4 DNS<sup>\*</sup>. In particular, SGS-D with  $\alpha = 1.5$  predicts too little mixing.

Overall, we find that all SGS models clearly improve the accuracy of the coarse-resolution simulations in capturing mixing in the lock-exchange system. We also see that the performance of some models is not consistent for all the  $Re$  investigated. For instance, SGS-D exhibits a dependence on the parameter  $\alpha$ , which was not observed in our previous study (Özgökmen et al., 2009). It appears that the higher  $Re$  regime is breaking a new barrier here. The change in the domain aspect ratio also seems to include a more complex interaction between stably- and unstably-stratified mixing in the system. Based on the errors  $\eta$  listed in Table 5, the overall conclusion is that most SGS models prove to be beneficial. This conclusion implies a strategy of conducting LES with an ensemble of SGS models, instead of relying on a single one.

### 5.3. Large eddy simulations for $Re = 10^5$ and $Re = 10^6$

In this section, we use the LES models investigated in Section 5.2 to gain insight into mixing in the lock-exchange problem at higher  $Re$  for which DNS results are not available. It is clear from the LES study presented in the previous section that, although

most LES models prove to be beneficial, it is not possible to claim that a specific SGS model has a consistent and significant advantage over the others. Therefore, we select an ensemble of SGS models. Specifically, we select SGS-G, which has fared well for all  $Re$ , together with SGS-R, SGS-E and SGS-F, which have yielded good results for the higher  $Re$  cases. We also increase the resolution for LES to mid-res1 (Table 2). Although these are significant computations, they are still feasible on high-end workstations and do not require major computational resources. We test all LES models at  $Re = 10^5$  and  $Re = 10^6$ .

Results from mid-res1 LES with four different SGS at  $Re = 10^5$  are plotted in Fig. 13. We note a reasonable agreement in all LES runs. While some differences exist during the period of  $7 \leq t^* \leq 12$ , they are relatively small. All LES models yield more mixing than high-res4 DNS<sup>\*</sup> at  $Re = 3 \times 10^4$ . The same set of numerical simulations is repeated for  $Re = 10^6$  (Fig. 14).

Based on this ensemble of LES results, we compute their averaged  $RPE^*(t^*)$ , and present it together with the previous DNS computations so that we can now cover the mixing taking place in this lock-exchange problem over the range of  $10^3 \leq Re \leq 10^6$  (Fig. 15). Within the integration period, we see a significant increase from  $Re = 10^3$  to  $Re = 10^4$ , and also from  $Re = 10^4$  to  $Re = 10^5$ , but a relatively smaller change from  $Re = 10^5$  to  $Re = 10^6$ . In all cases, when  $Re$  is increased, mixing initiates earlier in the simulation and increases at a higher rate. Thus, at the end of the integration,  $RPE^*(t^* = 13.5)$  changes from 0.097 for  $Re = 10^3$  to 0.162 for  $Re = 10^6$ , which represents a 67% increase.

## 6. Summary and conclusions

Turbulent mixing of water masses of different temperatures and salinities is an important process for both coastal and large-scale ocean circulation. Recent advances in computational power and numerical methods have created new avenues for modeling turbulent mixing. In this study, we build upon the

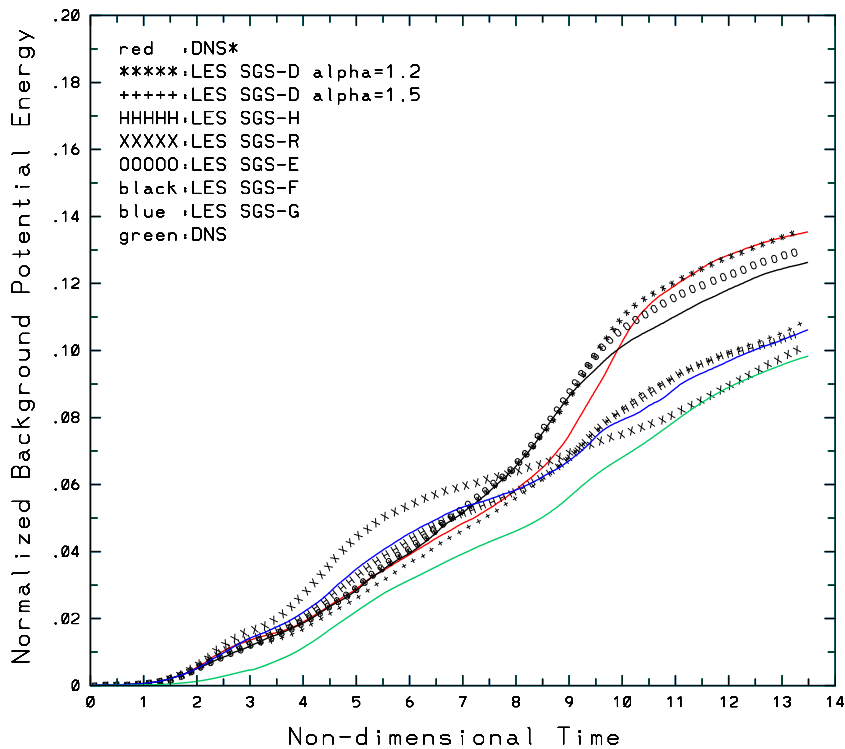


Fig. 10. Time evolutions of the normalized background potential energy  $RPE^*(t^*)$  from low-res1 LES with different SGS models for  $Re = 3 \times 10^3$ . Reference curves from low-res1 DNS\* and mid-res1 DNS are shown in red and green curves, respectively.

insight gained from our two prior investigations (Özgökmen et al., 2007, 2009), and continue to thoroughly test the performance of LES for stratified mixing. The main objectives of this study are: (i)

to investigate the performance of different LES models at high  $Re$ ; and (ii) to study how mixing varies as a function of  $Re$ . This numerical study is particularly relevant to oceanic flows, where

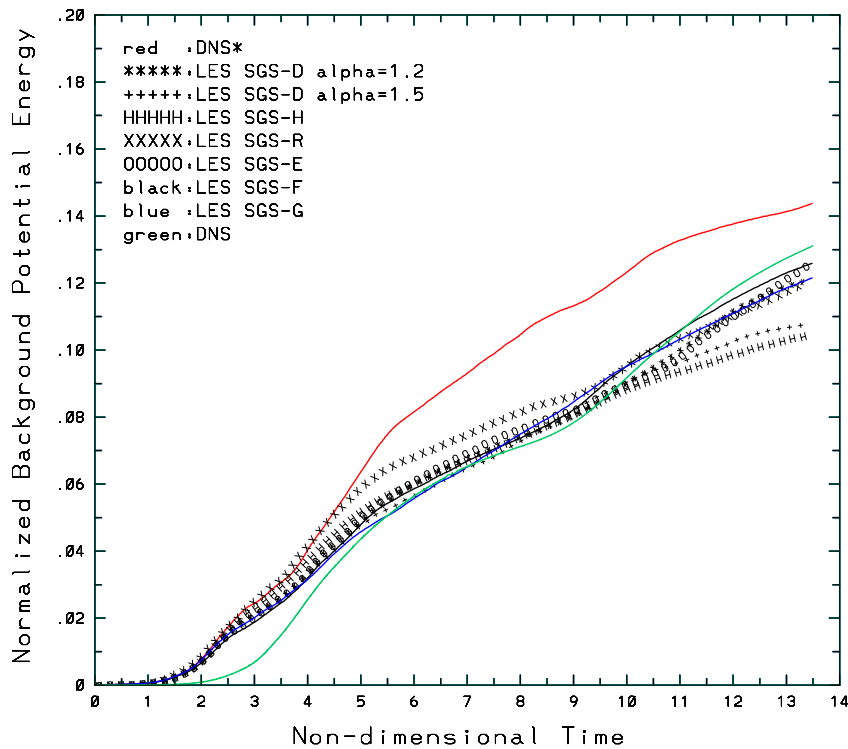
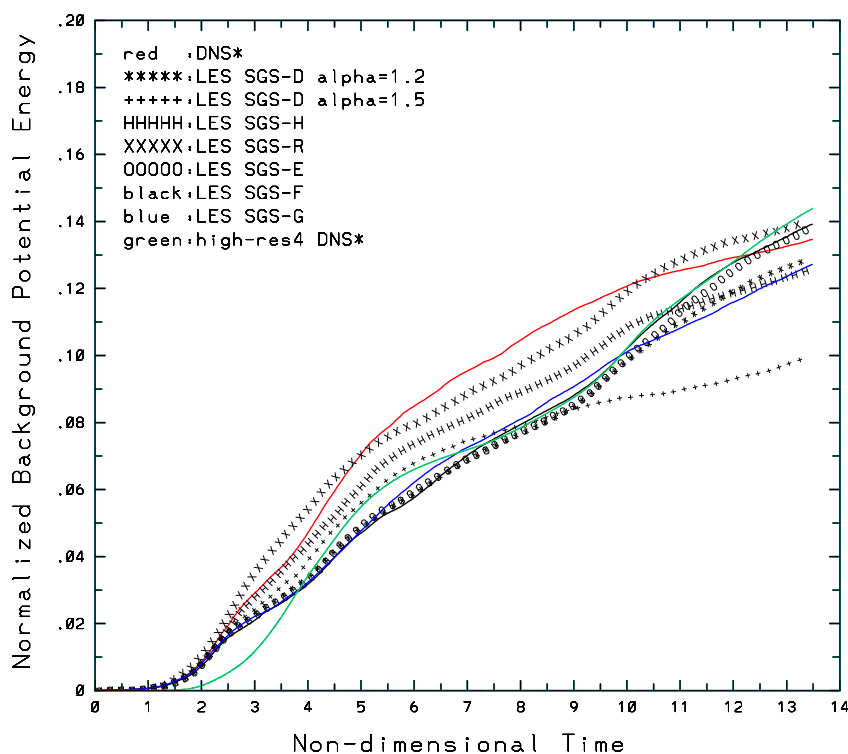


Fig. 11. Time evolutions of the normalized background potential energy  $RPE^*(t^*)$  from low-res1 LES with different SGS models for  $Re = 10^4$ . Reference curves from low-res1 DNS\* and high-res2 DNS are shown in red and green curves, respectively. (For interpretation of the references to color in this figure legend, the reader is referred to the web version of this article.)



**Fig. 12.** Time evolutions of the normalized background potential energy  $RPE^*(t^*)$  from low-res1 LES with different SGS models for  $Re = 3 \times 10^4$ . Reference curves from low-res1 DNS\* and high-res4 DNS\* are shown in red and green curves, respectively. (For interpretation of the references to color in this figure legend, the reader is referred to the web version of this article.)

**Table 5**

Error metric  $\eta$  (%) from all LES. Bold values indicates worse results than DNS\*, while italic values indicates significant improvements identified with subjective criterion of  $\eta \leq 67\%$ .

SGS model	$Re = 3 \times 10^3$	$Re = 10^4$	$Re = 3 \times 10^4$
SGS-D $\alpha = 1.2$	<b>110</b>	27	41
SGS-D $\alpha = 1.5$	40	39	<b>109</b>
SGS-H	46	49	58
SGS-R	60	45	90
SGS-E	<b>101</b>	29	30
SGS-F	90	21	28
SGS-G	45	26	45

mixing takes place at a wide range of  $Re$ . We also note that the investigation in (i) is necessary in order to be able to use LES for  $Re$  for which DNS data is not available.

We continue to work with the lock-exchange problem. As opposed to configuring a complex oceanic problem, in which uncertainties in the initial conditions, boundary conditions, forcing and observational data may obscure the exact amount of mixing, the lock-exchange problem is described by unambiguous and simple initial and boundary conditions, and serves as an ideal setting for conducting systematic tests.

Our strategy for a path to high  $Re$  is as follows. For gradually increasing  $Re$ , we conduct convergence tests with increasing spatial resolution in order to identify the DNS. The background potential energy, which accurately quantifies irreversible mixing in an enclosed system, is used as the metric of comparison in *a posteriori* testing of LES. The simulations are conducted at 9 different resolutions, ranging from 232,897 to 76,431,937 points, and increasing with the  $Re$ . We start with  $Re = 10^3$ , where this system shows first signs of turbulence, and gradually increase the  $Re$  by a factor of about three, namely  $Re = 3 \times 10^3$ ,  $Re = 10^4$  and  $Re = 3 \times 10^4$ . At least two cases of close agreement are required for convergence. By the time our tests with

$Re = 3 \times 10^4$  are finished, it is clear that much larger computations than those feasible with our resources are necessary to attain DNS at higher  $Re$ . We resort to LES to obtain estimates of mixing for  $Re > 3 \times 10^4$ . To assess the accuracy of these LES models, however, we first evaluate them at  $Re$  for which benchmark DNS results are available. We use two general classes of SGS models, namely eddy-viscosity and approximate deconvolution types. Six different SGS models are tested, all based on combinations of formulations of the dynamic Smagorinsky, *Ri*-dependent Smagorinsky and Rational models. All computations are carried out using the spectral element code Nek5000 (Fischer, 1997), which offers minimal diffusion and dispersion errors, and high scalability that is critical for this study. Overall, results from 50 numerical simulations are described here.

We find that the mixing in this system at  $Re = 10^3$  is readily captured with a direct approach (no SGS modeling) and the differences among results from different spatial resolutions are so small that LES testing is not needed. At  $Re = 3 \times 10^3$ , the system starts creating a complex range of turbulent coherent structures. The mixing curve, however, remains virtually unchanged with respect to that from the lower  $Re$ . When the  $Re$  is increased further, we encounter fully-developed turbulence, and significant increases in the background potential energy  $RPE^*$  emerge. Various SGS models are tested using DNS results from  $Re = 3 \times 10^3$ ,  $Re = 10^4$  and  $Re = 3 \times 10^4$ . It is found that all SGS models show an improvement with respect to DNS\*. It is not possible, however, to identify a clear and consistent winner. Therefore, an ensemble of SGS models is used to get estimates of mixing at  $Re = 10^5$  and  $Re = 10^6$ . Overall, we obtain a measure of mixing taking place in this lock-exchange problem during the integration period over a  $Re$  range of three orders of magnitude. The larger the  $Re$  is, the faster the system starts mixing and the higher the  $RPE^*$  is at the end of integrations:  $RPE^*(t^* = 13.5) = 0.097$  for  $Re = 10^3$  and  $Re = 3 \times 10^3$ ,  $RPE^*(t^* = 13.5) = 0.131$  for  $Re = 10^4$ ,  $RPE^*(t^* = 13.5) = 0.144$  for  $Re = 3 \times 10^4$ .  $RPE^*(t^* =$

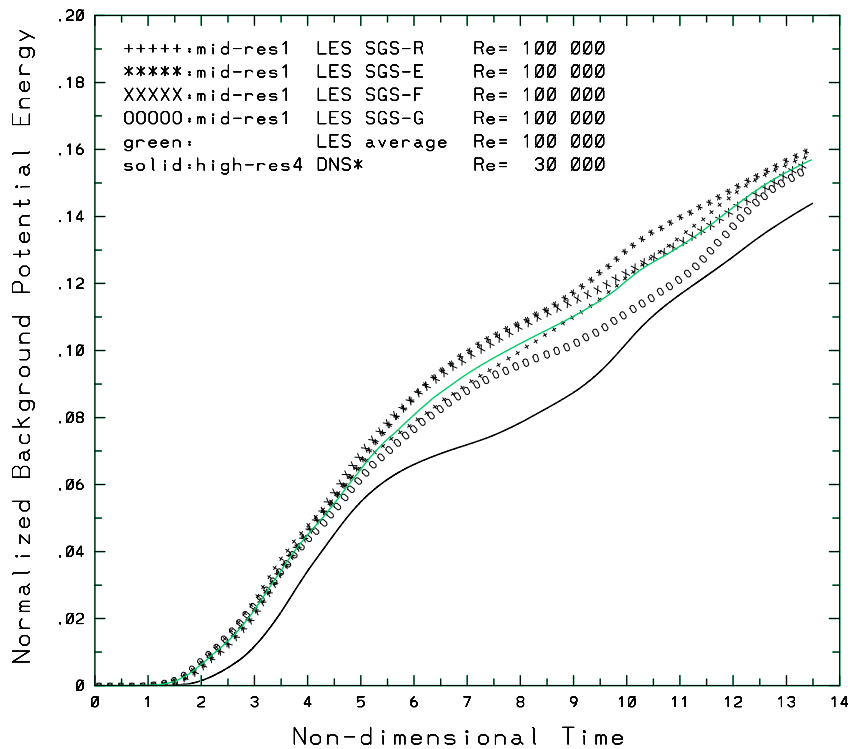


Fig. 13. Time evolutions of the normalized background potential energy  $RPE^*(t^*)$  from mid-res1 LES with SGS-R, SGS-E, SGS-F and SGS-G models, as well as their average, for  $Re = 10^5$ . The curve from high-res4 DNS\* for  $Re = 3 \times 10^4$  is shown for reference.

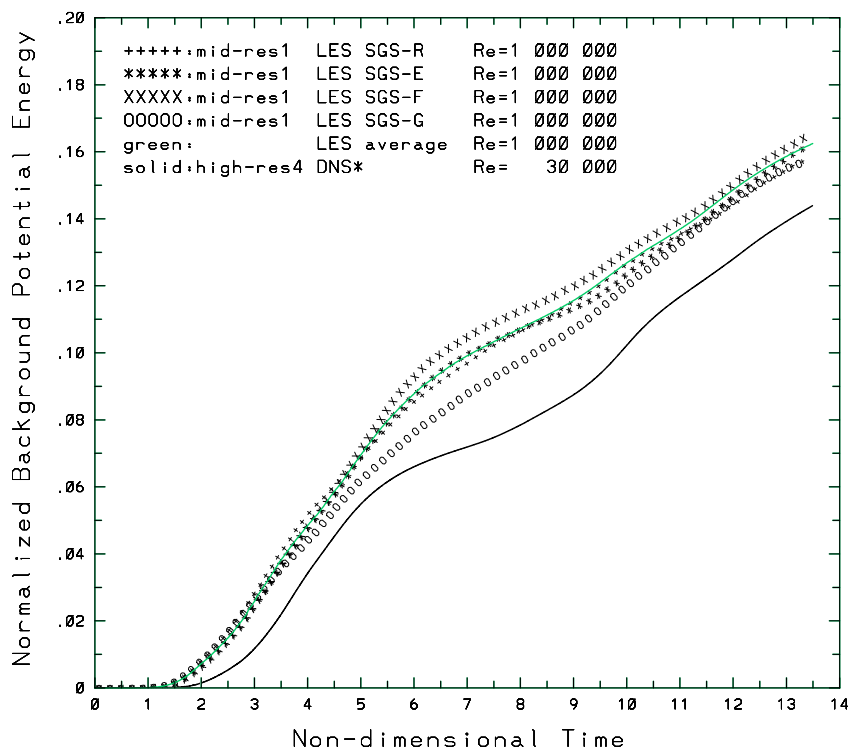


Fig. 14. Time evolutions of the normalized background potential energy  $RPE^*(t^*)$  from mid-res1 LES with SGS-R, SGS-E, SGS-F and SGS-G models, as well as their average, for  $Re = 10^6$ . The curves from mid-res1 DNS\* for  $Re = 10^6$  is shown for reference.

13.5) = 0.157 for  $Re = 10^5$  and  $RPE^*(t^* = 13.5) = 0.162$  for  $Re = 10^6$ . Thus, it is found that the mixing increases by about 67% when the  $Re$  is increased a 1000-fold.

Of course, our conclusions for the highest  $Re$  tested ( $Re = 10^5$  and  $Re = 10^6$ ) must await further DNS results in order to be fully validated. The computations in this study demonstrate once again

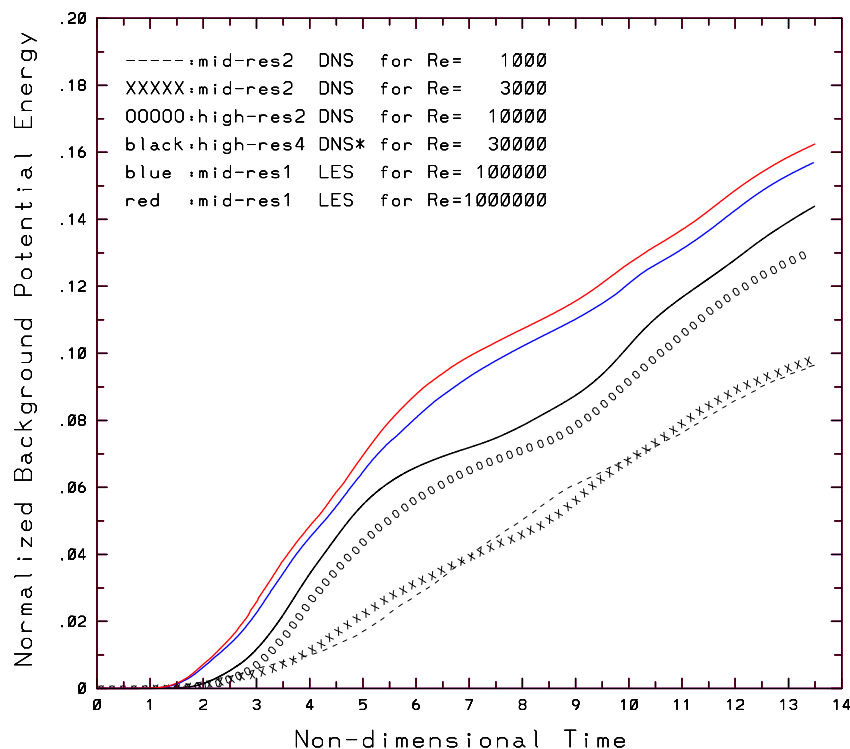


Fig. 15. Comparison of the time evolutions of normalized background potential energy  $RPE^*(t^*)$  from DNS and averaged LES for  $10^3 \leq Re \leq 10^6$ .

the challenge of modeling mixing accurately in high- $Re$  stratified flows characteristic of oceanic cases.

### Acknowledgments

We greatly appreciate the support of National Science Foundation via grants OCE-0620661 and OCE-0620464 under the Collaborative Mathematics and Geoscience (CMG) initiative. Most computations were carried out on the University of Miami's high-performance computing center (<http://www.ccs.miami.edu/>). We would like to thank the center's director Nicholas Tsironemas, HPC director Joel Zysman, and Ashwanth Srinivasan for these resources and convenient access, and especially Zongjun Hu for his continuous daily assistance and help. A significant and important portion of the computations were completed on SystemX at Virginia Tech's advanced research computing center (<http://www.arc.vt.edu>). We thank Dr. Terry Herdman and Michael Snow for their help. We also thank the two anonymous reviewers for their constructive comments, which helped improve the manuscript.

### References

- Baumert, H., Peters, H., 2004. Turbulence closure, steady state, and collapse into waves. *J. Phys. Oceanogr.* 34, 505–512.
- Baumert, H., Simpson, J., Sündermann, J., 2005. *Marine Turbulence*. Cambridge University Press, Cambridge, UK.
- Benjamin, T.B., 1968. Gravity currents and related phenomena. *J. Fluid Mech.* 31, 209–248.
- Berselli, L., Iliescu, T., Layton, W., 2005. *Mathematics of Large Eddy Simulation of Turbulent Flows*. Springer-Verlag.
- Britter, R.E., Simpson, J.E., 1978. Experiments on the dynamics of a gravity current head. *J. Fluid Mech.* 88, 223–240.
- Burchard, H., Baumert, H., 1995. On the performance of a mixed-layer model based on the  $k-\epsilon$  turbulence closure. *J. Geophys. Res.* 100, 8523–8540.
- Burchard, H., Bolding, K., 2001. Comparative analysis of four second-moment turbulence closure models for the oceanic mixed layer. *J. Phys. Oceanogr.* 31, 1943–1968.
- Cantero, M.I., Balachandar, S., Garcia, M., Ferry, J.R., 2006. Direct numerical simulations of planar and cylindrical density currents. *J. Appl. Mech.* 73, 923–930.
- Cantero, M.I., Lee, J.R., Balachandar, S., Garcia, M., 2007. On the front velocity of gravity currents. *J. Fluid Mech.* 586, 1–39.
- Canuto, V., Cheng, Y., Howard, A., 2007. Non-local ocean mixing mode and a new plume model for deep convection. *Ocean Modell.* 16, 28–46.
- Canuto, V.M., Howard, A.M., Cheng, Y., Esau, I.N., 2008. Stably stratified flows: a model with no  $Ri(cr)$ . *J. Atmos. Sci.* 65, 2437–2447.
- Canuto, V.M., Howard, A., Cheng, Y., Dubovikov, M.S., 2001. Ocean turbulence. Part I: one-point closure model momentum and heat vertical diffusivities. *J. Phys. Oceanogr.* 31, 1413–1426.
- Cao, C., Holm, D.D., Titi, E.S., 2005. On the Clark- $\alpha$  model of turbulence: global regularity and long-time dynamics. *J. Turbul.*, 1468–5248 6, 11 (Electronic).
- Carati, D., Winkelmann, G., Jeanmart, H., 2001. On the modeling of the subgrid-scale and filtered-scale stress tensors in large-eddy simulation. *J. Fluid Mech.* 441, 119–138.
- Chang, Y., Xu, X., Özgökmen, T., Chassignet, E., Peters, H., Fischer, P., 2005. Comparison of gravity current mixing parameterizations and calibration using a high-resolution 3d nonhydrostatic spectral element model. *Ocean Modell.* 10, 342–368.
- Clark, R., Ferziger, J., Reynolds, W., 1979. Evaluation of subgrid scale models using an accurately simulated turbulent flow. *J. Fluid Mech.* 91, 1–16.
- Deville, M., Fischer, P., Mund, E., 2002. *High-order Methods for Incompressible Fluid Flow*, vol. 9 of Cambridge Monographs on Applied and Computational Mathematics. Cambridge University Press, Cambridge, ISBN 0-521-45309-7.
- Dörnbrack, A., 1998. Turbulent mixing by breaking gravity waves. *J. Fluid Mech.* 375, 113–141.
- Dryja, M., Widlund, O.B., 1987. An additive variant of the Schwarz alternating method for the case of many subregions. Technical Report Technical Report 339. Dept. Computer Science, Courant Institute.
- Ferron, B., Mercier, H., Speer, K., Gargett, A., Poltzin, K., 1998. Mixing in the romanche fracture zone. *J. Phys. Oceanogr.* 28, 1929–1945.
- Fischer, P., Gottlieb, D., 1997. On the optimal number of subdomains for hyperbolic problems on parallel computers. *Int. J. Supercomp. Appl. High Perf. Comp.* 11, 65–76.
- Fischer, P., Mullen, J., 2001. Filter-based stabilization of spectral element methods. *C. R. Acad. Sci. Paris Sér. I Math.*, 0764-4442 332 (3), 265–270.
- Fischer, P.F., 1997. An overlapping Schwarz method for spectral element solution of the incompressible Navier–Stokes equations. *J. Comp. Phys.* 133, 84–101.
- Fischer, P.F., Miller, N.I., Tufo, H.M., 2000. An overlapping Schwarz method for spectral element simulation of three-dimensional incompressible flows. In: Luskin, P.B.M. (Ed.), *Parallel Solution of Partial Differential Equations*. Springer-Verlag, pp. 159–181.
- Fischer, P.F., Ronquist, E.M., 1994. Spectral element methods for large scale parallel Navier–Stokes calculation. *Comput. Methods Appl. Mech. Eng.* 116, 69.

- Frisch, U., 1995. *Turbulence, The Legacy of A.N. Kolmogorov*. Cambridge University Press, Cambridge.
- Galdi, G., Layton, W., 2000. Approximation of the larger eddies in fluid motions. II. A model for space-filtered flow. *Math. Models Methods Appl. Sci.*, 0218–2025 10 (3), 343–350.
- Germano, M., Piomelli, U., Moin, P., Cabot, W., 1991. A dynamic subgrid-scale eddy viscosity model. *Phys. Fluids A* 3, 1760–1765.
- Gibson, C., Nabatov, V., Ozmidov, R., 1993. Measurements of turbulence and fustil turbulence near Ampere seamount. *Dyn. Atmos. Oceans* 19, 175–204.
- Hacker, J., Linden, P.F., Dalziel, S.B., 1996. Mixing in lock–release gravity currents. *Dyn. Atmos. Oceans* 24 (1–4), 183–195.
- Hallworth, M.A., Huppert, H.E., Phillips, J.C., Sparks, R.S.J., 1996. Entrainment into two-dimensional and axisymmetric turbulent gravity currents. *J. Fluid Mech.* 308, 289–311.
- Hallworth, M.A., Phillips, J.C., Huppert, H.E., Sparks, R.S.J., 1993. Entrainment in turbulent gravity currents. *Nature* 362, 829–831.
- Härtel, C., Meiburg, E., Necker, F., 2000. Analysis and direct numerical simulation of the flow at a gravity-current head. Part 1. Flow topology and front speed for slip and no-slip boundaries. *J. Fluid Mech.* 418, 189–212.
- Huppert, H.E., Simpson, J.E., 1980. The slumping of gravity currents. *J. Fluid Mech.* 99, 785–799.
- Ilicak, M., Özgökmen, T., Özsoy, E., Fischer, P., 2009. Non-hydrostatic modeling of exchange flows across complex geometries. *Ocean Modell.* 29, 159–175.
- Ilicak, M., Özgökmen, T.M., Peters, H., Baumert, H.Z., Iskandarani, M., 2008. Performance of two-equation turbulence closures in three-dimensional simulations of the Red Sea overflow. *Ocean Modell.* 24, 122–139.
- Iliescu, T., Fischer, P., 2003. Large Eddy Simulation of turbulent channel flows by the Rational LES model. *Phys. Fluids* 15 (10), 3036–3047.
- Iliescu, T., Fischer, P., 2004. Backscatter in the Rational LES model. *Comput. Fluids* 35 (5–6), 783–790.
- John, V., 2004. Analytical and numerical results for a class of LES models. *Large Eddy Simulation of Turbulent Incompressible Flows*, vol. 34 of Lecture Notes in Computational Science and Engineering. Springer-Verlag, Berlin, ISBN 3-540-40643-3.
- John, V., 2005. An assessment of two models for the subgrid scale tensor in the Rational LES model. *J. Comp. Appl. Math.* 173, 57–80.
- Kantha, L.H., Clayson, C.A., 1994. An improved mixed layer model for geophysical applications. *J. Geophys. Res.* 99, 252355–252366.
- Kantha, L.H., Clayson, C.A., 2000. *Small Scale Processes in Geophysical Flows*. Academic Press, New York.
- Katopodes, F., Street, R., Ferziger, J., 2000. Subfilter-scale scalar transport for large-eddy simulation. In: 14th Symposium on Boundary Layer and Turbulence. American Meteorological Society, pp. 472–475.
- Klaassen, G.P., Peltier, W.R., 1989. The role of transverse secondary instabilities in the evolution of free shear layers. *J. Fluid Mech.* 202, 367–402.
- Klaassen, G.P., Peltier, W.R., 1991. The influence of stratification on secondary instability in free shear layers. *J. Fluid Mech.* 227, 71–106.
- Kunze, E., Toole, J., 1997. Tidally driven vorticity, diurnal shear, and turbulence atop Fieberling Seamount. *J. Phys. Oceanogr.* 27, 2663–2693.
- Lavelle, J., Lozovatsky, I., Smith, D., 2004. Tidally induced turbulent mixing at Irving Seamount – Modeling and measurements. *Geophys. Res. Lett.* 31 (L10308). doi:10.1029/2004GL019706.
- Ledwell, J., Montgomery, E., Polzin, K., Schmitt, R., St. Laurent, L., Toole, J., 2000. Evidence for enhanced mixing over rough topography in the abyssal ocean. *Nature* 403, 179–182.
- Leonard, A., 1974. Energy cascade in large eddy simulations of turbulent fluid flows. *Adv. Geophys.* 18A, 237–248.
- Lottes, J.W., Fischer, P.F., 2005. Hybrid multigrid/Schwarz algorithms for the spectral element method. *J. Sci. Comput.* 24 (1), 45–78.
- Lueck, R., Mudge, T., 1997. Topographically induced mixing around a shallow seamount. *Science* 276, 1831–1833.
- Maday, Y., Patera, A.T., 1989. Spectral element methods for the Navier–Stokes equations. In: Noor, A.K. (Ed.), *State of the Art Surveys in Computational Mechanics*. ASME, pp. 71–143.
- Maday, Y., Patera, A.T., Rønquist, E.M., 1990. An operator-integration-factor splitting method for time-dependent problems: application to incompressible fluid flow. *J. Sci. Comput.* 10, 496–508.
- Mellor, G.L., Yamada, T., 1982. Development of a turbulence closure model for geophysical fluid problems. *Rev. Geophys.* 30, 851–875.
- Meneveau, C., Lund, T., Cabot, W., 1996. A Lagrangian dynamic subgrid-scale model of turbulence. *J. Fluid Mech.* 319, 353–385.
- Miles, J.W., 1961. On the stability of heterogeneous shear flows. *J. Fluid Mech.* 10, 496–508.
- Moum, J., Caldwell, D., Nash, J., Gunderson, G., 2002. Observations of boundary mixing over the continental slope. *J. Phys. Oceanogr.* 32, 2113–2130.
- Nabatov, V., Ozmidov, R., 1988. A study of turbulence over underwater mountains in the Atlantic Ocean. *Oceanology* 28, 210–217 (in Russian).
- Özgökmen, T., Fischer, P., 2008. On the role of bottom roughness in overflows. *Ocean Modell.* 20, 336–361.
- Özgökmen, T., Fischer, P., Johns, W., 2006. Product water mass formation by turbulent density currents from a high-order nonhydrostatic spectral element model. *Ocean Modell.* 12, 237–267.
- Özgökmen, T., Iliescu, T., Fischer, P., 2009. Large eddy simulation of stratified mixing in a three-dimensional lock-exchange system. *Ocean Modell.* 26, 134–155.
- Özgökmen, T., Iliescu, T., Fischer, P., Srinivasan, A., Duan, J., 2007. Large eddy simulation of stratified mixing in two-dimensional dam-break problem in a rectangular enclosed domain. *Ocean Modell.* 16, 106–140.
- Özgökmen, T.M., Fischer, P.F., Duan, J., Iliescu, T., 2004a. Three-dimensional turbulent bottom density currents from a high-order nonhydrostatic spectral element model. *J. Phys. Oceanogr.* 34 (9), 2006–2026.
- Özgökmen, T.M., Fischer, P.F., Duan, J., Iliescu, T., 2004b. Entrainment in bottom gravity currents over complex topography from three-dimensional nonhydrostatic simulations. *Geophys. Res. Lett.* 31 (L13212). doi:10.1029/2004GL020186.
- Patera, A., 1984. A spectral element method for fluid dynamics: laminar flow in a channel expansion. *J. Comp. Phys.* 54, 468–488.
- Peters, H., Gregg, M., Sanford, T., 1995. Detail and scaling of turbulent overturns in the Pacific Equatorial Undercurrent. *J. Geophys. Res.* 100, 18349–18368.
- Peters, H., Johns, W.E., 2005. Mixing and entrainment in the Red Sea outflow plume. Part ii: turbulence characteristics. *J. Phys. Oceanogr.* 35, 584–600.
- Poltzin, K., Toole, J., Ledwell, J., Schmitt, R., 1997. Spatial variability of turbulent mixing in the abyssal ocean. *Science* 276, 93–96.
- Pope, S., 2000. *Turbulent Flows*. Cambridge University Press, Cambridge, ISBN 0-521-59886-9.
- Porté-Agel, F., Meneveau, C., Parlange, M.B., 2000. A scale-dependent dynamic model for large-eddy simulation: application to a neutral atmospheric boundary layer. *J. Fluid Mech.* 0022-1120 415, 261–284.
- Price, J.F., Baringer, M.O., 1994. Outflows and deep water production by marginal seas. *Prog. Oceanogr.* 33, 161–200.
- Rohr, J.J., Itsweire, E.C., Helland, K.N., Atta, C.W.V., 1988. Growth and decay of turbulence in stably stratified shear flow. *J. Fluid Mech.* 195, 77–111.
- Rottman, J.W., Simpson, J.E., 1983. Gravity currents produced by instantaneous releases of a heavy fluid in a rectangular channel. *J. Fluid Mech.* 135, 95–110.
- Sagaut, P., 2006. *Large Eddy Simulation for Incompressible Flows*. Scientific Computation. Springer-Verlag, Berlin.
- Schlatter, P., Stolz, S., Kleiser, L., 2004. LES of transitional flows using the approximate deconvolution model. *Int. J. Heat Fluid Flow* 25, 549–558.
- Schumann, U., 1975. Subgrid scale model of finite difference simulations of turbulent flows in plane channels and annuli. *J. Comp. Phys.* 18, 376–404.
- Shin, J.O., Dalziel, S.B., Linden, P.F., 2004. Gravity currents produced by lock exchange. *J. Fluid Mech.* 521, 1–34.
- Simpson, J.E., 1979. The dynamics of the head of a gravity current advancing over a horizontal surface. *J. Fluid Mech.* 94, 477–495.
- Smagorinsky, J., 1963. General circulation experiments with the primitive equations. *Mon. Weather Rev.* 91, 99–164.
- Stevens, B., Moeng, C.-H., Sullivan, P., 1998. Entrainment and subgrid lengthscales in large-eddy simulations of atmospheric boundary layer flows. In: Kerr, R.M., Kimura, Y. (Eds.), *Developments in Geophysical Turbulence*. Kluwer, pp. 253–269.
- Stolz, S., Adams, N., 1999. An approximate deconvolution procedure for large-eddy simulation. *Phys. Fluids* 11 (7), 1699–1701.
- Stolz, S., Schlatter, P., Kleiser, L., 2005. High-pass filtered eddy-viscosity models for large-eddy simulations of transitional and turbulent flow. *Phys. Fluids* 17, 065103.
- Thorpe, S., 2005. *The Turbulent Ocean*. Cambridge University Press, New York.
- Thurnherr, A., 2006. Diapycnal mixing associated with an overflow in a deep submarine canyon. *Deep Sea Res. II* 53, 194–206.
- Thurnherr, A., Laurent, L.S., Speer, K., Toole, J., Ledwell, J., 2004. Mixing associated with sills in a canyon on the mid-ocean ridge flank. *J. Phys. Oceanogr.* 35, 1370–1381.
- Thurnherr, A., Speer, K., 2003. Boundary mixing and topographic blocking on the Mid-Atlantic Ridge in the South Atlantic. *J. Phys. Oceanogr.* 33, 848–862.
- Tseng, Y., Ferziger, J., 2001. Mixing and available potential energy in stratified flows. *Phys. Fluids* 13, 1281–1293.
- Tufo, H.M., Fischer, P., 2001. Fast parallel direct solvers for coarse grid problems. *J. Par. Dist. Comput.* 173, 431–471.
- Umlauf, L., Burchard, H., 2005. Second-order turbulence closure models for geophysical boundary layers: a review of recent work. *Cont. Shelf Res.* 25, 795–827.
- Warner, J.C., Sherwood, C.R., Arango, H.G., Signell, R.P., 2005. Performance of four turbulence closure methods implemented using a generic length scale method. *Ocean Modell.* 8, 81–113.
- Winckelmans, G., Wray, A., Vasilyev, O., Jeanmart, H., 2001. Explicit-filtering large-eddy simulations using the tensor-diffusivity model supplemented by a dynamic Smagorinsky term. *Phys. Fluids* 13, 1385–1403.
- Winters, K.B., Lombard, P.N., Riley, J.J., D’Asaro, E.A., 1995. Available potential energy and mixing in density-stratified fluids. *J. Fluid Mech.* 289, 115–128.
- Xu, X., Chang, Y., Peters, H., Özgökmen, T., Chassignet, E., 2006. Parameterization of gravity current entrainment for ocean circulation models using a high-order 3d nonhydrostatic spectral element model. *Ocean Modell.* 14, 19–44.